

RESEARCH ARTICLE | OCTOBER 04 2024

On the adaption of biological transport networks affected by complex domains

Yibao Li (李义宝)  ; Zhixian Lv (吕志贤)  ; Qing Xia (夏青)  



Physics of Fluids 36, 101906 (2024)

<https://doi.org/10.1063/5.0231079>



View
Online



Export
Citation

Articles You May Be Interested In

On the conservative phase-field method with the N-component incompressible flows

Physics of Fluids (January 2023)

The algorithm for constructing an efficient transport system in the simplest cell

AIP Conf. Proc. (September 2018)

Machine learning for autonomous vehicles

AIP Conf. Proc. (August 2024)



Physics of Fluids

Special Topic:

Recent Advances in Fluid Dynamics and its Applications

Guest Editors: B.Reddappa, B. Rushi Kumar, Sreedhara Rao Gunakala, Bijula Prabhakar Reddy

Submit Today!

 AIP
Publishing

On the adaption of biological transport networks affected by complex domains

Cite as: Phys. Fluids **36**, 101906 (2024); doi: [10.1063/5.0231079](https://doi.org/10.1063/5.0231079)

Submitted: 28 July 2024 · Accepted: 11 September 2024 ·

Published Online: 4 October 2024



View Online



Export Citation



CrossMark

Yibao Li (李义宝), ^{a)} Zhixian Lv (吕志贤), and Qing Xia (夏青) ^{b)}

AFFILIATIONS

School of Mathematics and Statistics, Xi'an Jiaotong University, Xi'an 710049, China

^{a)}Electronic mail: yibaoli@xjtu.edu.cn. URL: <http://gr.xjtu.edu.cn/web/yibaoli>

^{b)}Author to whom correspondence should be addressed: xiaqing151701@stu.xjtu.edu.cn

ABSTRACT

This paper aims to simulate and analyze scenarios involving obstacles and parasitic organisms during the growth of biological structures. We introduce an innovative model of biological transport networks in complex domains. By manipulating sources and sinks, we simulate two distinct types of domains. One obstructs nutrient transport without absorbing energy. The other one obstructs transport and absorbs energy. Our model adheres to the continuous functional energy dissipation law. Employing a Crank–Nicolson type method ensures second-order time accuracy. The phase field-based discrete system is decoupled, linear, and unconditionally stable, facilitating straightforward implementation of the algorithm. Our scheme maintains stability in addressing the stiffness of the hybrid system. Our research demonstrates that effective mathematical modeling and numerical methods can accurately simulate and analyze the growth of biological transport networks in complex domains.

Published under an exclusive license by AIP Publishing. <https://doi.org/10.1063/5.0231079>

I. INTRODUCTION

Biological transport networks are pervasive in nature,¹ exemplified by structures like leaf veins in plants,² the circulatory systems of mammals,³ and neural networks transmitting charges.⁴ They play pivotal roles across various domains, influencing traffic network design⁵ and significantly contributing to signal processing.⁶ Many natural and engineered phenomena occur within intricate geometric frameworks, spanning biological tissues,⁷ geological formations,⁸ and complex materials.⁹ Employing partial differential equations within these domains allows for more precise simulations of real-world scenarios, enhancing our understanding and predictive capabilities for practical challenges. In medicine, structures and processes within living organisms often exhibit intricate geometric shapes, evident in human organs and cell structures.¹⁰ Moreover, applying model solutions within complex domains aids in simulating physical processes in natural settings, such as atmospheric dynamics and hydrological models.¹¹

The biological transport networks within complex organisms navigate diverse domains, such as tumors,¹² plaques, or scar tissues,¹³ which significantly influence transport pathways¹⁴ and fluid dynamics.¹⁵ These obstacles alter fluid velocities, directions, and nutrient absorption, impacting overall flow efficiency and structural integrity. To maintain effective transport, networks optimize paths to minimize transport time and energy consumption, ensuring robustness and

redundancy against obstructions.¹⁶ The vascular system can form new vessels around blockages,¹⁷ while plant root systems navigate around soil obstacles to absorb water and nutrients.¹⁸ Accurately modeling these networks requires considering complex domains using high-dimensional, nonlinear models¹⁹ involving fluid dynamics, material transport, and energy consumption.²⁰ These simulations demand efficient numerical methods and significant computational resources to ensure stability and accuracy.^{21,22} Research on biological transport networks in complex domains aids in designing better treatment methods and agricultural practices, optimizing drug delivery in cancer treatment, and improving crop yields.²³

In recent years, significant advancements have been made in constructing and solving biological transport networks.²⁴ Fang *et al.* developed implicit and semi-implicit time discretizations for the Cai–Hu model, demonstrating unconditional energy decay and decay independent of mesh size in their proposed discretizations, which are crucial for biological transport network formation.²⁵ Models designed for complex domains have also seen notable developments.^{26,27} Anderson *et al.* introduced a high-order accurate algorithm for determining particular solutions to complex partial differential equations, effectively handling PDEs within intricate spatial contexts by convolving the volumetric source function with Green's function.²⁸ Costabal *et al.* developed a positional encoding mechanism for physics-informed neural

networks based on eigenfunctions of the Laplace–Beltrami operator, facilitating simulation and modeling in complex spatial domains by representing geometric shapes of objects in the input space.²⁹ Many models employ simplified assumptions to reduce computational complexity, potentially leading to discrepancies with real-world results.³⁰ Existing numerical methods may face stability and convergence issues³¹ when dealing with nonlinear and high-dimensional problems,³² making them less suitable for complex scenarios.^{33,34} Biological processes are influenced by multiple factors, and effectively integrating these factors and coupling them within models remains a challenge. While progress has been made in solving biological transport networks in complex domains, it remains a significant challenge in current research and applications, necessitating further study and technological innovation to overcome these difficulties.

The phase field model plays a crucial role in fields such as materials science,^{35,36} physics,^{37,38} triply periodic structures,^{39,40} and chemistry,⁴¹ with applications spanning topology optimization,^{42,43} and porous media.⁴⁴ This model serves as a powerful computational tool, enabling the simulation of microstructural evolution and complex pattern formations across various systems.⁴⁵ It captures the evolution of grain boundaries,^{46,47} offering insights into the mechanisms driving growth and the resulting microstructural properties.⁴⁸ For multicomponent fluid flow, Xia *et al.*⁴⁹ and Yang *et al.*⁵⁰ illustrated its utility in simulating the behavior of immiscible fluids. Additionally, the phase-field equation is applied in modeling complex domains.⁵¹ In studying ferroelectric perovskites, Dayal and Bhattacharya⁵² developed a phase-field method to explore domain patterns and their evolution in intricate geometries without assuming prior knowledge of geometry, electrode configurations, or dielectric properties. Moreover, Yang *et al.*⁵³ introduced a novel diffuse-interface phase-field model to effectively describe the dynamics of compound droplets in contact with solid objects, demonstrating superior capability in handling complex geometries. In the study of biological transport networks, understanding network formation in complex domains is crucial. Complex domains often introduce new pathways and branches that significantly distinguish them from simpler domains, where such intricate growth patterns do not emerge. Recent research⁵⁴ modified the phase-field model to incorporate auxin gradients, which are essential for regulating transport across phase boundaries and initiating branch development from the main network structure. To capture the influence of complex environments on biological transport networks, we will introduce an indicator function G , representing two distinct types of environmental complexity. This extension allows our model to simulate a wider range of realistic biological scenarios, expanding its scope of applications. In comparison to existing approaches, our method significantly advances the simulation of biological transport network growth in complex domains.

In this paper, we introduce an innovative model of biological transport networks designed to simulate and analyze scenarios involving obstacles and parasitic organisms during the growth of biological structures. The model integrates phase field theory with the Cai–Hu model, effectively simulating two complex environments. One obstructs nutrient transport without energy consumption. The other one behaves like a parasite, obstructing transport and absorbing energy. Developed based on the physical principles of biological transport processes, this novel model demonstrates adherence to the law of continuous energy dissipation for continuous functions. To ensure

numerical accuracy, we will employ the Crank–Nicolson method for temporal discretization. Despite using a semi-implicit time scheme, our algorithm remains stable in addressing stiffness issues in mixed systems. The discretization of the phase field-based system is decoupled and linear, exhibiting unconditional stability, which facilitates straightforward implementation and practical application. Our research highlights the feasibility of effective mathematical modeling and efficient numerical methods for simulating and analyzing the growth processes of biological transport networks in complex domains. The proposed model is rigorously validated for their energy dissipation characteristics and demonstrates excellent performance through various numerical tests.

The remainder of this paper is organized as follows. In Sec. II, we modify the total energy in complex domains and establish the governing equations for the phase-field-based biological transport network in complex domains. In Sec. III, we describe the second-order time accuracy discretization scheme based on the Crank–Nicolson method and rigorously prove the discrete energy dissipation. Section IV conducts various numerical tests through benchmark examples. Finally, concluding remarks are presented in Sec. V.

II. METHODOLOGY

In this section, we incorporate complex domains into the energy function of the phase field-based biological transport network, resulting in a partial differential equation model for biological network generation that accounts for energy dissipation in complex domains. We verify that the model conforms to the laws of energy dissipation.

A. Constructing a novel model for biological transport networks on complex domains

We define the conductance vector as $\mathbf{m}(\mathbf{x}, t) \in \Omega$, where Ω represents a bounded domain. The direction of \mathbf{m} indicates active transport direction, while $|\mathbf{m}|$ measures transport intensity. We denote hormone pressure as $p(\mathbf{x}, t)$, and we signify background permeability as $r(\mathbf{x})$. We represent diffusivity with K and drive network adaptation using C . We define the metabolic constant as α and the metabolic rate of the organism as γ . We introduce G to denote the complex domain, where G ranges between [0, 1]. $G = 0$ indicates complete blockage, halting substance transport entirely, isolating nutrients. This scenario applies to domains lacking effective transport channels or occupied by parasitic organisms. When $G = 1$, it signifies maximum permeability or flux within the biological network, indicating fully open channels allowing unrestricted substance passage. The value of G reflects permeability and activity levels within veins or vasculature, representing different physiological states and functional characteristics within the biological system. According to Murray's law,⁵⁵ we consider the original energy cost functional \mathcal{E}_M as follows:

$$\mathcal{E}_M = \frac{1}{2} \int_{\Omega} \left(K|G\nabla \mathbf{m}|^2 + \frac{\alpha}{\gamma} G|\mathbf{m}|^{2\gamma} + CG|\mathbf{m} \cdot \nabla p|^2 + CrG|\nabla p|^2 \right) d\mathbf{x}, \quad (1)$$

where the first term $K|G\nabla \mathbf{m}|^2$ represents the entropy cost associated with active transport. The second term $\frac{\alpha}{\gamma} G|\mathbf{m}|^{2\gamma}$ reflects the material and metabolic energy cost of maintaining active transport or constructing the transport network edges. The last term $CG|\mathbf{m} \cdot \nabla p|^2 + CrG|\nabla p|^2$ represents the average energy cost for all different states

with fluctuating fluxes. This model drives canalization by coupling hormone transport with the adaptation process. For modeling biological transport networks in complex domains, we employ the phase-field model. Drawing on mathematical insights from leaf vein distribution,⁵⁶ the reaction–diffusion model, which incorporates auxin gradient properties, provides insights into network formation. The temporal variation of auxin concentration depends on the balance between diffusion and generation. We begin with the Ginzburg–Landau energy:

$$\mathcal{E}_\phi = \int_{\Omega} G \left(\frac{F(\phi)}{\varepsilon^2} + \frac{1}{2} |\nabla \phi|^2 \right) dx, \quad (2)$$

where $F(\phi) = 0.25\phi^2(1-\phi)^2$ and $\varepsilon > 0$ represents the interface thickness of vessel walls. The design variable ϕ ranges between $[0, 1]$, not limited to binary values 0 or 1. An interface layer proportional to ε replaces the hypersurface between leaf veins and nutrients. To characterize the topology of nutrient flow guided by conductance, we introduce a convection term

$$\mathcal{E}_C = \int_{\Omega} G |\mathbf{m} \cdot \nabla \phi|^2 dx. \quad (3)$$

Combining the metabolic cost energy with the Ginzburg–Landau energy, the modified total energy is

$$\begin{aligned} \mathcal{E} = \mathcal{E}_M + \mathcal{E}_\phi + \mathcal{E}_C = & \frac{1}{2} \int_{\Omega} \left(K |G \nabla \mathbf{m}|^2 + \frac{\alpha}{\gamma} G |\mathbf{m}|^{2\gamma} \right. \\ & \left. + CG |\mathbf{m} \cdot \nabla p|^2 + CrG |\nabla p|^2 \right) dx + \frac{\zeta}{2} \int_{\Omega} G |\mathbf{m} \cdot \nabla \phi|^2 dx \\ & + \int_{\Omega} G \left(\frac{F(\phi)}{\varepsilon^2} + \frac{1}{2} |\nabla \phi|^2 \right) dx, \end{aligned} \quad (4)$$

where $\zeta > 0$ is a parameter controlling the convective effect on conductivity. From the constrained gradient flows of the energy functional (4), we derive the equation as follows:

$$\frac{\partial \phi}{\partial t} = - \frac{\delta \mathcal{E}}{\delta \phi}, \quad (5)$$

whereby the variational derivative of the energy function with respect to ϕ gives us

$$\begin{aligned} \left(\frac{\delta \mathcal{E}}{\delta \phi}, \psi \right)_{L_2} = & \frac{d}{d\eta} \mathcal{E}(p, \mathbf{m}, \phi + \eta\psi) \Big|_{\eta=0} \\ = & \int_{\Omega} G \left(\frac{F'(\phi)}{\varepsilon^2} - \Delta \phi \right) \psi dx + \zeta \int_{\Omega} G (\mathbf{m} \otimes \mathbf{m}) \nabla \phi \cdot \nabla \psi dx \\ = & \int_{\Omega} G \left(\frac{F'(\phi)}{\varepsilon^2} - \Delta \phi \right) \psi - \zeta \nabla \cdot (G (\mathbf{m} \otimes \mathbf{m}) \cdot \nabla \phi) \psi dx \\ & + \zeta \int_{\partial\Omega} (\mathbf{n} \cdot G (\mathbf{m} \otimes \mathbf{m}) \cdot \nabla \phi) \psi ds \\ = & \int_{\Omega} G \left(\frac{F'(\phi)}{\varepsilon^2} - \Delta \phi \right) - \zeta \nabla \cdot (G (\mathbf{m} \otimes \mathbf{m}) \cdot \nabla \phi) \psi dx \end{aligned}$$

where the boundary condition $\mathbf{n} \cdot G (\mathbf{m} \otimes \mathbf{m}) \cdot \nabla \phi = 0$ is used. Gradient-driven mechanisms regulating production, diffusion, and differentiation gradients⁵⁷ can pair with reaction–diffusion equations. Constant parameters for diffusion transport and production

coordinate global information with vein formation. Thus, vein formation can be obtained through the proposed gradient flow model, providing opportunities for interaction between different biological tissue sections. The modified parameter \mathbf{m} can be obtained through the following gradient flow:

$$\frac{\partial \mathbf{m}}{\partial t} = - \frac{\delta \mathcal{E}}{\delta \mathbf{m}}, \quad (6)$$

whereby the variational derivative of the energy function with respect to \mathbf{m} yields vector-valued conductive functions

$$\begin{aligned} \left(\frac{\delta \mathcal{E}}{\delta \mathbf{m}}, \mathbf{g} \right)_{L_2} = & \frac{d}{d\eta} \mathcal{E}(p, \mathbf{m} + \eta \mathbf{g}, \phi) \Big|_{\eta=0} \\ = & \int_{\Omega} (-K \nabla \cdot (G^2 \nabla \mathbf{m}(\mathbf{x}, t)) + \alpha G |\mathbf{m}(\mathbf{x}, t)|^{2(\gamma-1)} \mathbf{m}(\mathbf{x}, t) \\ & - C(G \mathbf{m}(\mathbf{x}, t) \cdot \nabla p(\mathbf{x}, t)) \nabla p(\mathbf{x}, t) \\ & - \zeta (G \mathbf{m}(\mathbf{x}, t) \cdot \nabla \phi(\mathbf{x}, t)) \nabla \phi(\mathbf{x}, t)) \cdot \mathbf{g} dx. \end{aligned}$$

Thus, we can modify the original governing system as follows:

$$\begin{aligned} \frac{\partial \phi}{\partial t} (\mathbf{x}, t) = & \nabla \cdot (G \nabla \phi(\mathbf{x}, t)) - G \frac{F'(\phi(\mathbf{x}, t))}{\varepsilon^2} \\ & + \zeta \nabla \cdot (G (\mathbf{m}(\mathbf{x}, t) \otimes \mathbf{m}(\mathbf{x}, t)) \nabla \phi(\mathbf{x}, t)), \end{aligned} \quad (7a)$$

$$-\nabla \cdot (G(r(\mathbf{x})I + \mathbf{m}(\mathbf{x}, t) \otimes \mathbf{m}(\mathbf{x}, t)) \nabla p(\mathbf{x}, t)) = S(\mathbf{x}), \quad (7b)$$

$$\begin{aligned} \frac{\partial \mathbf{m}}{\partial t} (\mathbf{x}, t) = & C(G \mathbf{m}(\mathbf{x}, t) \cdot \nabla p(\mathbf{x}, t)) \nabla p(\mathbf{x}, t) \\ & + \zeta (G \mathbf{m}(\mathbf{x}, t) \cdot \nabla \phi(\mathbf{x}, t)) \nabla \phi(\mathbf{x}, t) \\ & - \alpha G |\mathbf{m}(\mathbf{x}, t)|^{2(\gamma-1)} \mathbf{m}(\mathbf{x}, t) \\ & + K \nabla \cdot (G^2 \nabla \mathbf{m}(\mathbf{x}, t)). \end{aligned} \quad (7c)$$

Here, I is the identity matrix. We use $S(\mathbf{x})$ to represent the distribution of sources and sinks in tissue, which is specified as a datum. Moreover, we observe that the homogeneous Neumann boundary condition imposes the global mass balance

$$\int_{\Omega} S(\mathbf{x}) dx = 0, \quad (8)$$

as a necessary condition to ensure the solvability of Eq. (7b). In our study, we develop two distinct types of source terms $S(\mathbf{x})$ to simulate various scenarios impacting biological transport networks and ensure they satisfy condition (8). For partial damage to plant leaves or interactions between plant roots and rocks, energy transfer within the complex region is hindered by physical or environmental constraints.⁵⁸ Energy cannot be transferred within the complex region; however, biological energy in the growth areas outside the complex region can be transferred normally, and the energy absorption capability of the entire region remains consistent. Therefore, we designed the first type of source term, which addresses scenarios involving local damage or external environmental influences, expressed as follows:

$$S(\mathbf{x}) = E(\mathbf{x}) - \bar{E}, \quad (9)$$

where $E(\mathbf{x}) \geq 0$ is a transition function used to generate $S(\mathbf{x})$, and \bar{E} represents the average value of $E(\mathbf{x})$. This captures the phenomenon of energy transfer being obstructed due to local disturbances or

environmental influences. For biological transport network growth in complex domains where parasitic organisms invade the host and extract energy, involving interactions between biological growth and energy absorption in such environments, energy cannot be effectively transferred within the complex region and is also absorbed by these areas. The growth of the biological transport network is influenced by the presence of complex domains. Thus, we designed the expression for the second type of source term as follows:

$$S(\mathbf{x}) = E(\mathbf{x}) - \frac{\bar{E}}{1 - \bar{G}}(1 - G(\mathbf{x})), \quad (10)$$

where \bar{G} represents the average value of $G(\mathbf{x})$. In Eq. (10), when $G(\mathbf{x}) = 1$, $S(\mathbf{x}) = E(\mathbf{x})$, whereas when $G(\mathbf{x}) = 0$, $S(\mathbf{x}) = E(\mathbf{x}) - \bar{E}/(1 - \bar{G})$. This configuration simulates a scenario where energy is absorbed by the complex region, impacting the growth of the biological transport network. By introducing these two source terms, our model aims to more comprehensively capture the interactions between biological systems and their environment. The first source term reflects how local damage or obstacles hinder energy transfer, while the second source term simulates how energy absorption by complex entities influences biological growth. This detailed approach facilitates the simulation of interactions between biological systems and their environment. We will discuss the impact of these source terms on the growth of the biological transport network in complex domains in subsequent evaluations. Based on the modified system Eqs. (7), we can obtain the following energy dissipation law. The governing equations (7) preserve the energy production rate as follows:

$$\frac{\partial \mathcal{E}}{\partial t} = \int_{\Omega} -|\mathbf{m}_t|^2 d\mathbf{x} + \int_{\Omega} -|\phi_t|^2 d\mathbf{x} \leq 0. \quad (11)$$

By taking the derivative formulation of the modified energy Eq. (4) with respect to time and taking the L^2 inner product of Eq. (7a) with ϕ_t , of Eq. (7c) with \mathbf{m}_t , and substituting Eq. (7b) into the derivation functional, the following energy dissipation law can be obtained:

$$\begin{aligned} \frac{\partial \mathcal{E}}{\partial t} &= \int_{\Omega} \left(K(G\nabla \mathbf{m}) \cdot (G\nabla \mathbf{m}_t) + \alpha G |\mathbf{m}|^{2\gamma-1} \frac{\mathbf{m}}{|\mathbf{m}|} \cdot \mathbf{m}_t \right. \\ &\quad \left. + CG(\mathbf{m} \cdot \nabla p) \cdot (\mathbf{m}_t \cdot \nabla p) + CG(\mathbf{m} \cdot \nabla p) \cdot (\mathbf{m} \cdot \nabla p_t) \right. \\ &\quad \left. + CrG\nabla p \cdot \nabla p_t \right) d\mathbf{x} + \int_{\Omega} G\left(\frac{F'(\phi)}{\varepsilon^2}\right) \cdot \phi_t + \nabla \phi \cdot \nabla \phi_t d\mathbf{x} \\ &\quad + \int_{\Omega} \left(\zeta G(\mathbf{m} \cdot \nabla \phi) \cdot (\mathbf{m}_t \cdot \nabla \phi) + \zeta G(\mathbf{m} \cdot \nabla \phi) \cdot (\mathbf{m} \cdot \nabla \phi_t) \right) d\mathbf{x} \\ &= \int_{\Omega} -K\nabla \cdot (G^2 \nabla \mathbf{m}) \cdot \mathbf{m}_t + \alpha G |\mathbf{m}|^{2(\gamma-1)} \mathbf{m} \cdot \mathbf{m}_t - \zeta G(\mathbf{m} \cdot \nabla \phi) \\ &\quad \times \nabla \phi \cdot \mathbf{m}_t - C(\mathbf{Gm} \cdot \nabla p) \nabla p \cdot \mathbf{m}_t + C(G(rI + \mathbf{m} \otimes \mathbf{m}) \nabla p) \cdot \nabla p_t \\ &\quad + G\left(\frac{F'(\phi)}{\varepsilon^2}\right) \cdot \phi_t - \zeta \nabla \cdot (G(\mathbf{m} \otimes \mathbf{m}) \nabla \phi) \cdot \phi_t - \nabla \cdot (G\nabla \phi) \cdot \phi_t d\mathbf{x} \\ &\quad + \int_{\partial\Omega} KG^2 \mathbf{n} \cdot \nabla \mathbf{m}_t + \mathbf{Cn} \cdot G(rI + \mathbf{m} \otimes \mathbf{m}) \cdot \nabla p_t \\ &\quad + \zeta \mathbf{n} \cdot G(\mathbf{m} \otimes \mathbf{m}) \cdot \nabla \phi \phi_t d\mathbf{s}, \end{aligned}$$

where the following boundary conditions have been applied as: $\mathbf{n} \cdot \nabla \mathbf{m}_t = 0$, $\mathbf{n} \cdot G(rI + \mathbf{m} \otimes \mathbf{m}) \cdot \nabla p = 0$, and $\mathbf{n} \cdot G(\mathbf{m} \otimes \mathbf{m}) \cdot \nabla \phi = 0$. Therefore, we are able to obtain

$$\frac{\partial \mathcal{E}}{\partial t} = \int_{\Omega} -|\mathbf{m}_t|^2 d\mathbf{x} + \int_{\Omega} -|\phi_t|^2 d\mathbf{x} \leq 0.$$

The proof is completed.

III. NUMERICAL SOLUTIONS

The numerical solution of our model for biological transport networks in complex domains employs second-order accurate spatial discretization and Crank–Nicolson time discretization. We discretize the bounded domain $\Omega = [0, L_x] \times [0, L_y] \subset \mathbb{R}^2$ into a grid $\Omega_d = \{(x_i, y_j) : 1 \leq i \leq N_x, 1 \leq j \leq N_y\}$, where both N_x and N_y are even integers. The grid points (x_i, y_j) are positioned at $x_i = (i - 0.5)h$ and $y_j = (j - 0.5)h$, with a uniform grid spacing h given by $h = L_x/N_x = L_y/N_y$. Let \mathbf{m}_{ij}^n represent the numerical approximation of $\mathbf{m}(x_i, y_j, n\Delta t)$, where Δt is the time step. Similarly, the discrete forms of $\phi(x_i, y_j, n\Delta t)$ and $p(x_i, y_j, n\Delta t)$ are defined in the same manner. The cell vertices are located at $(x_{i+\frac{1}{2}}, y_{j+\frac{1}{2}}) = (ih, jh)$. The discrete gradient operator $\nabla_d \phi_{ij}$ is expressed as $(D_x \phi_{i+\frac{1}{2}j}, D_y \phi_{ij+\frac{1}{2}})$, where $D_x \phi_{i+\frac{1}{2}j} = (\phi_{i+1,j} - \phi_{i,j})/h$ and $D_y \phi_{ij+\frac{1}{2}} = (\phi_{i,j+1} - \phi_{i,j})/h$. The discrete Laplacian operator $\Delta_d \phi_{ij}$ is given by $(\phi_{i-1,j} + \phi_{i+1,j} + \phi_{i,j-1} + \phi_{i,j+1} - 4\phi_{i,j})/h^2$. Additionally, we define discrete inner products and norms as follows: $(\phi, \psi)_d = h^2 \sum_{i=1}^{N_x} \sum_{j=1}^{N_y} \phi_{ij} \psi_{ij}$, $(\nabla_d \phi, \nabla_d \psi)_d = h^2 \sum_{i=1}^{N_x} \sum_{j=1}^{N_y} (D_x \phi_{i+\frac{1}{2}j} D_x \psi_{i+\frac{1}{2}j} + D_y \phi_{ij+\frac{1}{2}} D_y \psi_{ij+\frac{1}{2}})$, $\|\phi\|_d^2 = (\phi, \phi)_d$, $\|\nabla_d \phi\|_d^2 = (\nabla_d \phi, \nabla_d \phi)_d$, $\|\nabla_d \mathbf{m}\|_d^2 = \|D_x \mathbf{m}_1\|_d^2 + \|D_y \mathbf{m}_1\|_d^2 + \|D_x \mathbf{m}_2\|_d^2 + \|D_y \mathbf{m}_2\|_d^2$. To achieve second-order accuracy in both time and space, we utilize standard central difference discretization and the Crank–Nicolson scheme for the governing equations

$$\begin{aligned} \frac{\phi^{n+1} - \phi^n}{\Delta t} &= -\xi^{n+\frac{1}{2}} \frac{G \delta F(\tilde{\phi}^{n+\frac{1}{2}})}{\varepsilon^2 \delta \phi} + \nabla_d \cdot (G \nabla_d \phi^{n+\frac{1}{2}}) \\ &\quad + \zeta \nabla_d \cdot (G(\mathbf{m}^{n+\frac{1}{2}} \otimes \tilde{\mathbf{m}}^{n+\frac{1}{2}}) \nabla_d \phi^{n+\frac{1}{2}}), \end{aligned} \quad (12a)$$

$$(F(\phi^{n+1}) - F(\phi^n), \mathbf{1})_d = \xi^{n+\frac{1}{2}} \left(\frac{\delta F(\tilde{\phi}^{n+\frac{1}{2}})}{\delta \phi}, \phi^{n+1} - \phi^n \right)_d, \quad (12b)$$

$$-\nabla_d \cdot (G(r\mathbf{I} + \mathbf{m}^{n+\frac{1}{2}} \otimes \tilde{\mathbf{m}}^{n+\frac{1}{2}}) \nabla_d p^{n+\frac{1}{2}}) = S, \quad (12c)$$

$$\begin{aligned} \frac{\mathbf{m}^{n+1} - \mathbf{m}^n}{\Delta t} &= C \left(G \mathbf{m}^{n+\frac{1}{2}} \cdot \nabla_d p^{n+\frac{1}{2}} \right) \nabla_d \tilde{p}^{n+\frac{1}{2}} \\ &\quad + K \nabla_d \cdot (G^2 \nabla_d \mathbf{m}^{n+\frac{1}{2}}) - \alpha \|\mathbf{m}^{n+\frac{1}{2}}\|_d^{2(\gamma-1)} G \mathbf{m}^{n+\frac{1}{2}} \\ &\quad + \zeta \left(G \mathbf{m}^{n+\frac{1}{2}} \cdot \nabla_d \phi^{n+\frac{1}{2}} \right) \nabla_d \tilde{\phi}^{n+\frac{1}{2}}, \end{aligned} \quad (12d)$$

where $(\cdot)^{n+\frac{1}{2}} = 0.5(\cdot)^{n+1} + 0.5(\cdot)^n$, $(\cdot)^{n+\frac{1}{2}} = 1.5(\cdot)^n - 0.5(\cdot)^{n-1}$.

Remark 1. The system of Eqs. (12) employs a semi-implicit time discretization, with certain nonlinear terms in Eqs. (12c) and (12d) being treated implicitly. The application of the Lagrange multiplier approach in Eq. (12b) conforms to the framework of the Ginzburg–Landau gradient flow model, for which unique solvability has been demonstrated in prior studies.⁵⁹ The current system introduces additional complexities, making a straightforward proof of unique solvability challenging. The nonlinearity and coupling between variables introduce significant challenges in decoupling the equations to obtain a linearized system. This is further complicated by the semi-implicit nature of the time discretization, which may impact the solvability of the scheme.

Numerous research studies^{60,61} have explored the issue of unique solvability in biological transport systems, with a focus on the complex interactions between variables, including their coupling and nonlinear terms. Li et al. demonstrated the unique solvability in transport networks,⁶² and the methods they employed could potentially be extended to prove the unique solvability of our model. Due to space limitations, we will not provide the detailed proof here.

Remark 2. Let us define the discrete energy $\mathcal{E}_d(\phi^n, \mathbf{m}^n, p^n)$ is defined as follows:

$$\begin{aligned}\mathcal{E}_d(\phi^n, \mathbf{m}^n, p^n) = & \left(\frac{\alpha G}{2\gamma}, \|\mathbf{m}^n\|_d^2 \right)_d + \left(\frac{CG}{2}, \|\mathbf{m}^n \cdot \nabla_d p^n\|_d^2 \right)_d \\ & + \frac{K}{2} \|G \nabla_d \mathbf{m}^n\|_d^2 + \left(\frac{CrG}{2}, \|\nabla_d p^n\|_d^2 \right)_d \\ & + \left(\frac{\zeta G}{2}, \|\mathbf{m}^n \cdot \nabla_d \phi^n\|_d^2 \right)_d + \left(\frac{G}{\varepsilon^2}, F(\phi^n) \right)_d \\ & + \left(\frac{G}{2}, \|\nabla_d \phi^n\|_d^2 \right)_d.\end{aligned}\quad (13)$$

The discrete system given in Eqs. (12) preserves the energy dissipation law as follows:

$$\begin{aligned}\frac{\mathcal{E}_d(\phi^{n+1}, \mathbf{m}^{n+1}, p^{n+1}) - \mathcal{E}_d(\phi^n, \mathbf{m}^n, p^n)}{\Delta t} \\ = - \left\| \frac{\mathbf{m}^{n+1} - \mathbf{m}^n}{\Delta t} \right\|_d^2 - \left\| \frac{\phi^{n+1} - \phi^n}{\Delta t} \right\|_d^2 \leq 0.\end{aligned}$$

To ensure the fluency of the text, the proof process will be placed in Appendix. Readers can refer to the detailed derivation in Appendix.

Remark 3. In the model Eqs. (12), the nonlinear terms may cause high sensitivity of the solutions, potentially leading to instability. The Crank–Nicolson time discretization introduces a semi-implicit scheme, making the stability analysis more complex. Furthermore, different variables in the equations interact closely through coupling terms, requiring simultaneous consideration of the interactions among all variables during stability analysis. Therefore, conducting a theoretical analysis for convergence and error estimation is challenging. However, existing numerical studies have advanced the Crank–Nicolson approximation for phase-field equations, particularly in the context of solving the Ginzburg–Landau equation.⁶³ These studies have established a solid foundation for applying the Crank–Nicolson method to such equations, demonstrating the energy stability and convergence of the Crank–Nicolson scheme and providing valuable insights for further algorithm optimization and application.^{64,65} Additionally, there are articles related to biological transport networks that have conducted similar convergence and error estimation analyses based on energy dissipation.⁶⁶ The theoretical convergence and error analysis of our proposed scheme can be inspired by these approaches. Our algorithm demonstrates second-order convergence both spatially and temporally, as confirmed by our numerical validation.

IV. NUMERICAL TESTS

Numerical tests have been conducted, including a non-increasing discrete energy test, stability test, convergence testing, comparison of the effects of two types of sources in complex domain biological transport networks, multiple circular complex domain analysis, and examination of the impact of complex domain density and source shape on

biological structure growth. In this study, we select the computational domain as $\Omega = [0, 2] \times [0, 2]$, employing a 512×512 grid, and utilizing the following parameters for numerical simulations: $\varepsilon = 5h/(4\sqrt{2}\tanh(0.9))$, $r = 0.1$, $C = 50^2$, $K = 0.005^2$, $\alpha = 1$, $\gamma = 0.75$, $\zeta = 0.05$, and $t = 0.8h$, where $h = 1/256$. Before proceeding with the tests, let us introduce another crucial aspect into our model of biological transport networks in complex domains: the volumetric flux, denoted by \mathbf{v} . This variable correlates with the flow velocity within biological tissues and can be mathematically represented as $\mathbf{v} = -G(r\mathbf{I} + \mathbf{m} \otimes \mathbf{m})\nabla p$.

A. Impact of complex domains on biological network growth

In this section, we compare the effects of complex domains that affect the growth of the biological transport network, evaluating the effectiveness of our proposed new model. The initial conditions are specified as follows:

$$\begin{aligned}G(x, y) = & 0.5\tanh\left(\frac{|y - 1.156| + |x - 0.5| - 0.2}{2\sqrt{2}\varepsilon}\right) \\ & + 0.5\tanh\left(\frac{|y - 1.156| + |x - 1.5| - 0.2}{2\sqrt{2}\varepsilon}\right) \\ & + 0.5\tanh\left(\frac{|y - 0.734| + |x - 1| - 0.2}{2\sqrt{2}\varepsilon}\right) - 0.5, \\ \phi(x, y, 0) = & 0.5 - 0.5\tanh\left(\frac{|x - 1| - 0.075}{2\sqrt{2}\varepsilon}\right), \\ \mathbf{m}(x, y, 0) = & (\phi(x, y, 0)|y|, 0.4\phi(x, y, 0)|y|), \\ E(x, y) = & 1 - \tanh\left(\frac{\sqrt{(y - 1.85)^2 + (x - 1)^2} - 0.15}{2\sqrt{2}\varepsilon}\right), \\ S(x, y, 0) = & E(x, y) - \bar{E}, \quad p(x, y, 0) = 0,\end{aligned}\quad (14)$$

where $\bar{E} = \sum_{i=1}^{N_x} \sum_{j=1}^{N_y} E(x_i, y_j)/(N_x \times N_y)$. In the absence of complex domains, branches exhibit uniform growth, gradually developing finer branches as fluid diffusion progresses. Figures 1(a) and 1(b) demonstrate that the presence of complex domains forces branches to navigate around them, significantly influencing the direction and pace of network expansion and delaying the development of finer branches, particularly in the bottom domain.

Without complex domains, pressure gradient values are uniformly distributed, with higher values at the ends of the main branches and lower values within the branches due to direct suppression of perpendicular transport across phase boundaries. This results in minimal internal transport effects, illustrated in Fig. 1(c). The inability of the main phase to grow into complex domains leads to noticeable shape changes. Increased pressure gradients around complex domains indicate their substantial influence on pressure distribution. The velocity of the main phase exceeds that of the tissue phase due to permeation pressure effects on phase boundaries, as depicted in Fig. 1(d). In the presence of complex domains, the main phase navigates around them during growth. These findings underscore the significant impact of complex domains on branch growth direction and speed, validating the efficacy of our proposed model in complex environments.

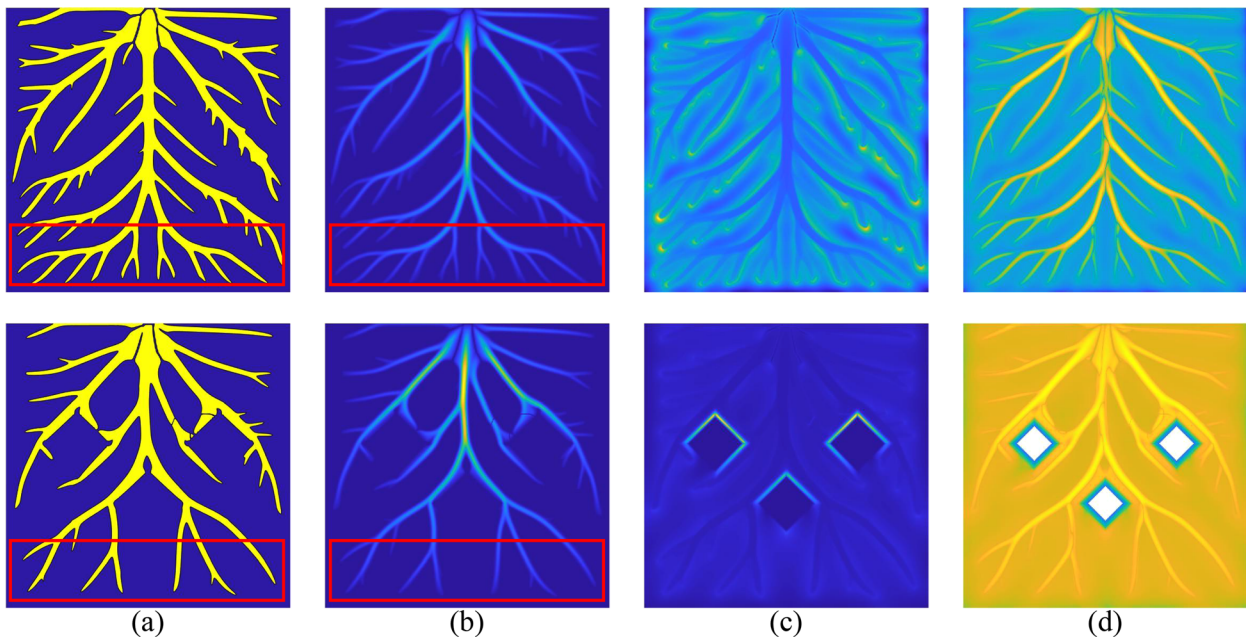


FIG. 1. The comparative results for scenarios without complex domains (top row) and with complex domains (bottom row). From (a) to (d), the results show the phase field ϕ , the L_2 norm of the conductance vector \mathbf{m} , the L_2 norm of ∇p , and the L_2 norm of fluid velocity \mathbf{v} in the log scale at specific time $t = 100$, respectively.

B. Non-increasing discrete energy test

We study the temporal evolution of the normalized discrete energy $\mathcal{E}_d(\phi^n, \mathbf{m}^n, p^n)/\mathcal{E}_d(\phi^0, \mathbf{m}^0, p^0)$. The initial conditions are chosen as follows:

$$\begin{aligned} G(x, y) &= 0.5 + 0.5 \tanh \left(\frac{\sqrt{(y-1)^2 + (x-1)^2} - 0.2}{2\sqrt{2}\varepsilon} \right), \\ \phi(x, y, 0) &= 0.5 - 0.5 \tanh \left(\frac{|x-y| - 0.075}{2\sqrt{2}\varepsilon} \right), \\ \mathbf{m}(x, y, 0) &= (0.5\phi(x, y, 0)(4 - |x| - |y|), 0.2\phi(x, y, 0)(4 - |x| - |y|)), \\ E(x, y) &= 1 - \tanh \left(\frac{\sqrt{(y-0.15)^2 + (x-0.15)^2} - 0.15}{2\sqrt{2}\varepsilon} \right), \\ S(x, y, 0) &= E(x, y) - \bar{E}, \quad p(x, y, 0) = 0, \end{aligned} \quad (15)$$

where $\bar{E} = \sum_{i=1}^{N_x} \sum_{j=1}^{N_y} E(x_i, y_j) / (N_x \times N_y)$. The analysis of the evolutionary process reveals that the structure grows outward under the influence of conductivity diffusion. Due to the inability to transport nutrients through complex domains, growth cannot penetrate these areas but instead bypasses them, continuing to transport nutrients. Throughout the growth process in the entire domain, the structure gradually converges, forming branches. Overly large branches begin to shrink, gradually developing into more refined biological transport branches. These refined branches effectively transmit energy to the required locations, thereby reducing energy waste. The subplots in Fig. 2 show the stable state of the biological network, where the structure remains unchanged during subsequent evolution. Using the same initial conditions specified in Eq. (15), we plot contour maps in Fig. 3

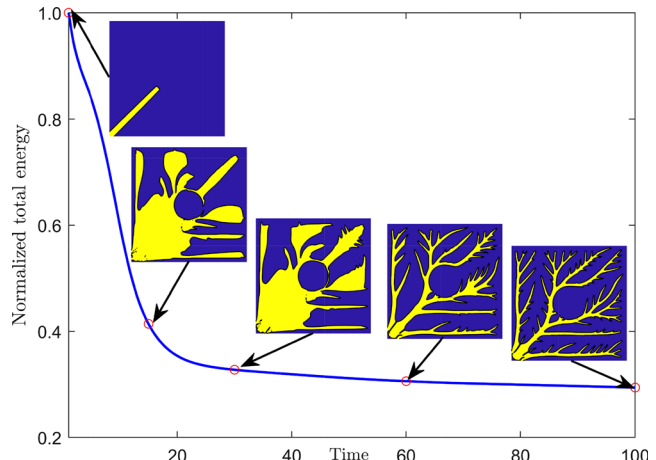


FIG. 2. Temporal evolution of the non-increasing energy of the proposed model. Note that the modified energy has been normalized by the initial energy. The inset figures are the morphology of phase field ϕ at specific times $t = 0, 15, 30, 60$, and 100 , respectively.

to illustrate the L_2 norms of the conductivity vector \mathbf{m} and ∇p at specific times $t = 0, 15, 30, 60$, and 100 , respectively. These time points correspond to the specific times $t = 15, 30, 60$, and 100 . The coupling term $(\mathbf{G}\mathbf{m} \cdot \nabla \phi)\nabla \phi$ directly inhibits transport in the direction perpendicular to the phase interface while reducing the impact on internal transport, thereby enhancing the stability of the numerical scheme. As shown in Fig. 3(a), the main trunk forms and gradually shrinks, with the structure growing around the complex domain as fluid diffuses.

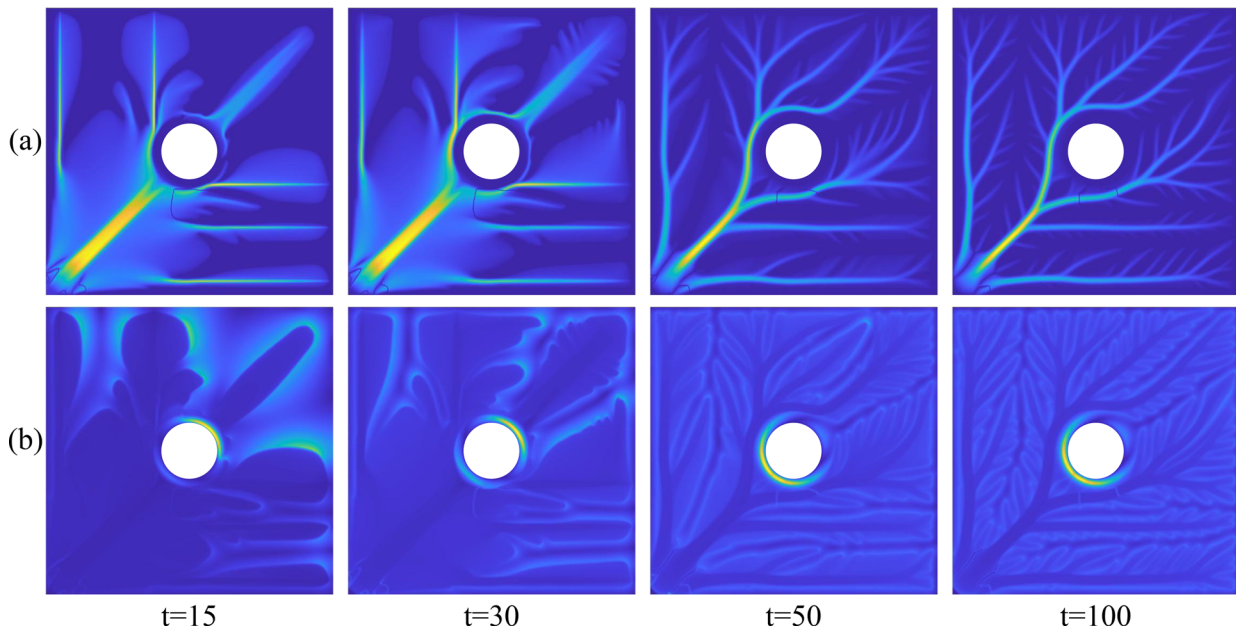


FIG. 3. The evolution results of the biological transport network in complex domains. (a) is the L_2 norm of the conductance vector \mathbf{m} and (b) is the L_2 norm of ∇p .

In **Fig. 3(b)**, it can be seen that the shrinkage of the main trunk is caused by osmotic pressure, with the osmotic pressure around the complex domain limiting the direction of growth while promoting relatively stable energy transmission paths within other domains. Under the influence of osmotic pressure at the phase interface, branches gradually form over time. The presence of such complex domains significantly affects the structural evolution of the biological network, forcing nutrients to bypass the complex domains and form branches around them. The evolutionary process demonstrates the adaptability of the biological network in different domains and its ability to optimize energy distribution.

C. Stability test

Our model incorporates both the convention term and the chemical potential term, thereby encompassing strong nonlinearities and high-order spatial derivatives. Explicit time integration schemes impose stringent time step limitations for stability. To validate the stability of our proposed method, we conducted numerical tests using time steps $\Delta t = 1, 0.1, 0.01$, and 0.001 . The initial conditions are set as follows:

$$G(x, y) = \frac{1}{2} \tanh \left(\frac{\sqrt{(y - 1.5)^2 + (x - 0.5)^2} - 0.3}{2\sqrt{2}\varepsilon} \right) + \frac{1}{2} \tanh \left(\frac{\sqrt{(y - 0.5)^2 + (x - 1.5)^2} - 0.3}{2\sqrt{2}\varepsilon} \right),$$

$$\phi(x, y, 0) = 0.5 - 0.5 \tanh \left(\frac{|x - y| - 0.075}{2\sqrt{2}\varepsilon} \right),$$

$$\mathbf{m}(x, y, 0) = (0.5\phi(x, y, 0)(4 - |x| - |y|), 0.2\phi(x, y, 0)(4 - |x| - |y|)),$$

$$E(x, y) = 1 - \tanh \left(\frac{\sqrt{(y - 0.15)^2 + (x - 0.15)^2} - 0.15}{2\sqrt{2}\varepsilon} \right),$$

$$S(x, y, 0) = E(x, y) - \bar{E}, p(x, y, 0) = 0,$$
(16)

where $\bar{E} = \sum_{i=1}^{N_x} \sum_{j=1}^{N_y} E(x_i, y_j) / (N_x \times N_y)$. In this test, we define the complex domain as two large circles. **Figure 4** compares the evolution of total energy over time, up to $t = 100$, for four different time steps.

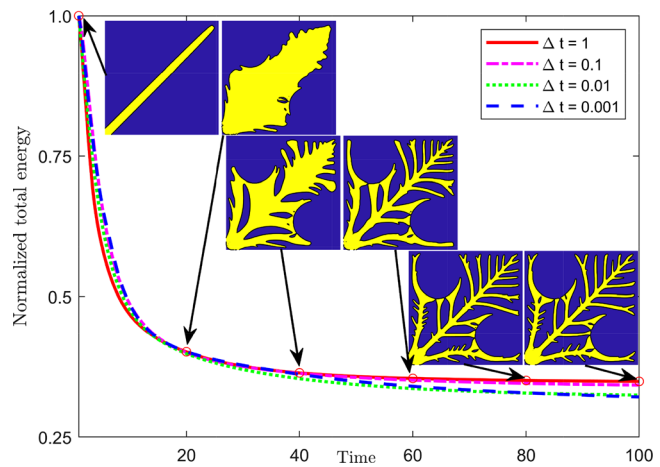


FIG. 4. Temporal evolution of the energy functional of the proposed model with four time step sizes of $\Delta t = 1, 0.1, 0.01$, and 0.001 until $T = 100$, respectively. Note that the modified energy has been normalized by the initial energy. The inset figures are the morphology of the phase field ϕ at specific times $t = 0, 20, 40, 60, 80$, and 100 , respectively. The subfigures are obtained with $\Delta t = 1$.

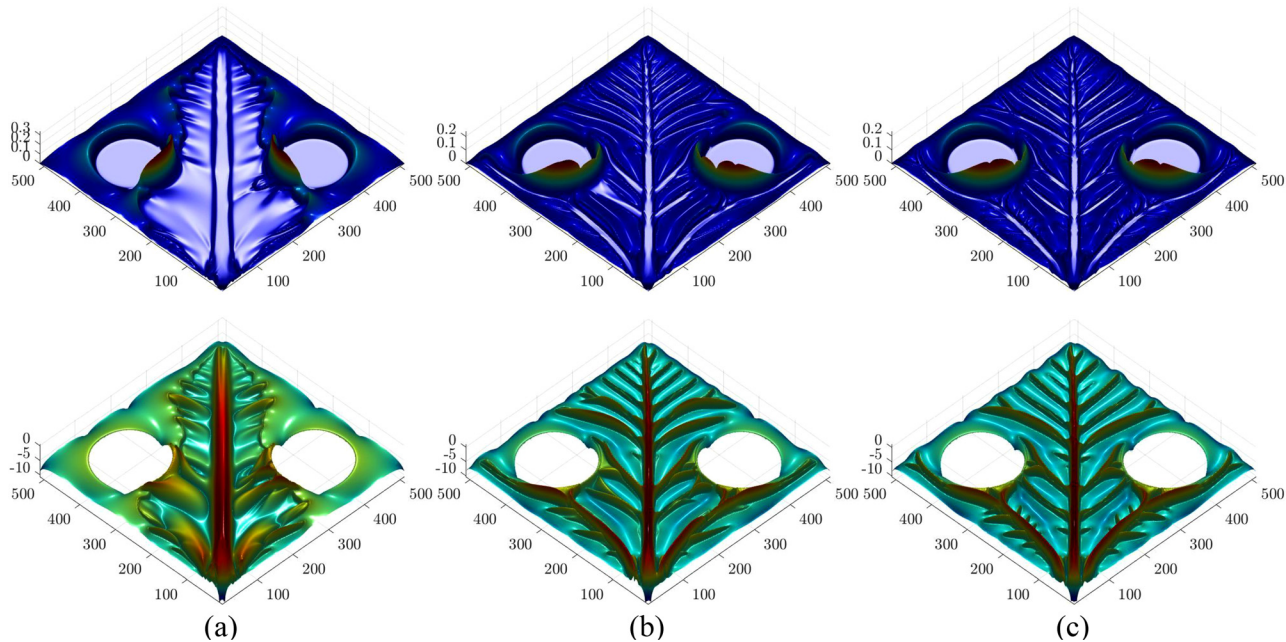


FIG. 5. The first and second rows show the L_2 norm of ∇p , and the L_2 norm of the fluid velocity \mathbf{v} on a logarithmic scale, respectively. From (a) to (c) display these results at specific times 20, 60 and 100, respectively.

All energy curves exhibit consistent decay without numerical solution divergence, indicating that our method supports the use of larger time steps. Although smaller time steps reduce truncation errors and yield more accurate results, particularly at $\Delta t = 0.001$, higher accuracy in numerical solutions can be achieved with these smaller steps. The inset of Fig. 4 illustrates the morphology of the phase field at times 0, 20, 40, 60, 80, and 100 with $\Delta t = 1$. In the initial growth phase, influenced by osmotic pressure, energy transport pathways are not fully formed, leading to a wide diffusion range. From the perspective of biological tissue generation and evolution, diffusion effects dominate in the early stages of the process. The first row of Fig. 5 shows significant pressure differentials around the complex domain, which impede the system's growth into this area. Subsequently, cross terms dominate during the stabilization process, ensuring network connectivity through the dissolution of nutrients between branches. The second row of Fig. 5 indicates that fluid velocity \mathbf{v} demonstrates nutrient transport from the main branch to the surroundings. However, this transport halts when encountering the complex domain due to the inability to transfer energy. The evolution and generation of the biological transport network over the complex domain confirm the convergence of the numerical solution and validate the applicability of larger time steps.

D. Convergence test

To assess the numerical accuracy of our method, we employ the Euler method within the domain $\Omega = [0, 2] \times [0, 2]$. Given the absence of an analytical solution, we establish reference solutions ϕ^{ref} , m_1^{ref} , m_2^{ref} , and p^{ref} using fine time steps or grid sizes to evaluate spatial and temporal accuracies. The initial conditions are specified as follows:

$$\begin{aligned} G(x, y) &= 0.5 + 0.5 \tanh\left(\frac{\sqrt{(y-1)^2 + (x-1)^2} - 0.15}{2\sqrt{2}\epsilon}\right), \\ \phi(x, y, 0) &= \sin(\pi x) \sin(\pi y), p(x, y, 0) = \cos(\pi x) \cos(\pi y), \\ m_1(x, y, 0) &= \cos(\pi x) \sin(\pi y), m_2(x, y, 0) = \sin(\pi x) \cos(\pi y), \quad (17) \\ E(x, y) &= 1 - \tanh\left(\frac{\sqrt{(y-0.15)^2 + (x-0.15)^2} - 0.15}{2\sqrt{2}\epsilon}\right), \\ S(x, y, 0) &= E(x, y) - \bar{E}, \end{aligned}$$

where $\bar{E} = \sum_{i=1}^{N_x} \sum_{j=1}^{N_y} E(x_i, y_j) / (N_x \times N_y)$. Homogeneous Neumann boundary conditions are applied for convergence testing. We employed decreasing temporal steps of $\Delta t = 1.6 \times 10^{-4}$, $\Delta t = 8 \times 10^{-5}$, and $\Delta t = 4 \times 10^{-5}$, along with a fine spatial size of $h = 1/512$, to verify second-order temporal accuracy. Reference solutions were computed with $\Delta t = 1 \times 10^{-5}$, defining the numerical error as $e_{i,\Delta t} := \phi_{i,\Delta t} - \phi_i^{\text{ref}}$. The convergence rate was evaluated using $\log_2(||e_{i,\Delta t}||_2 / ||e_{i,\Delta t/2}||_2)$. The results, summarized in Table I, confirm the second-order temporal accuracy based on system Eqs. (12). Subsequently, we used a fixed temporal step size of $\Delta t = 1 \times 10^{-5}$ to investigate spatial convergence up to $T = 0.1$. Spatial steps varied as $h = 1/128$, $h = 1/256$, and $h = 1/512$. The spatial error was defined as $e_{i,h} := \phi_{i,h} - \phi_i^{\text{ref}}$, and the spatial convergence rate was computed as $\log_2(||e_{i,h}||_2 / ||e_{i,h/2}||_2)$, relative to a reference solution obtained using $h = 1/1024$. Detailed numerical errors and spatial convergence results, presented in Table II, confirm the second-order spatial accuracy of our method.

TABLE I. Errors and convergence rates with different time steps for the conductance m_1 and m_2 , pressure p , and phase field ϕ .

Δt	Error				Order			
	m_1	m_2	p	ϕ	m_1	m_2	p	ϕ
1.6×10^{-4}	8.625×10^{-4}	6.986×10^{-4}	6.032×10^{-4}	9.862×10^{-4}	—	—	—	—
8.0×10^{-5}	2.178×10^{-4}	1.679×10^{-4}	1.493×10^{-4}	2.258×10^{-4}	1.99	2.04	2.01	2.09
4.0×10^{-5}	5.612×10^{-5}	4.115×10^{-5}	3.808×10^{-5}	5.533×10^{-5}	1.97	2.01	1.98	2.02

TABLE II. Errors and convergence rates with different spatial steps for the conductance m_1 and m_2 , pressure p , and phase field ϕ .

N	Error				Order			
	m_1	m_2	p	ϕ	m_1	m_2	p	ϕ
128	9.979×10^{-3}	8.496×10^{-3}	7.662×10^{-3}	8.219×10^{-3}	—	—	—	—
256	2.398×10^{-3}	2.189×10^{-3}	1.859×10^{-3}	2.076×10^{-3}	2.01	1.97	2.03	1.99
512	5.935×10^{-4}	5.365×10^{-4}	4.695×10^{-4}	4.891×10^{-4}	2.04	2.02	1.99	2.06

E. Comparing the results by two different sources and sinks

This test compares and analyzes energy transfer and the growth of biological structures in complex domains utilizing two types of sources and sinks initialized by Eqs. (9) and (10). Previous studies in this paper employed sources and sinks defined by Eq. (9). Initialization with Eq. (10) leads to energy absorption in complex domains, influencing the growth of biological transport networks. The evolution of

biological transport networks in these complex domains is simulated using the initial condition from Eq. (10) and additional conditions described in Eq. (15). During the initial stages of biological network growth, depicted in Fig. 6, energy diffuses outward, stimulating the growth of adjacent biological tissues. Energy absorption in complex domains redirects the predominant energy flow toward these areas, prompting the main biological structure to encircle them and impeding the formation of branches on the main stem. To illustrate the

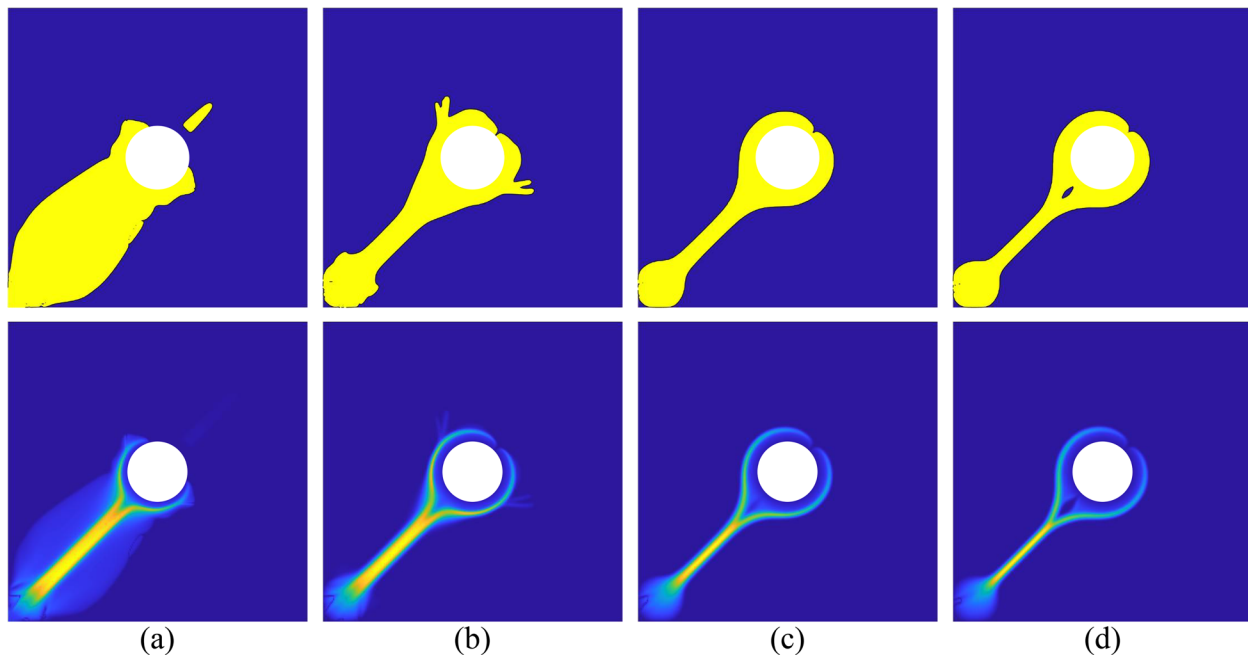


FIG. 6. The phase field variable ϕ and the L_2 norm of the conductance vector \mathbf{m} are depicted at specific times (a) $t = 15$, (b) $t = 30$, (c) $t = 50$, and (d) $t = 100$, respectively.

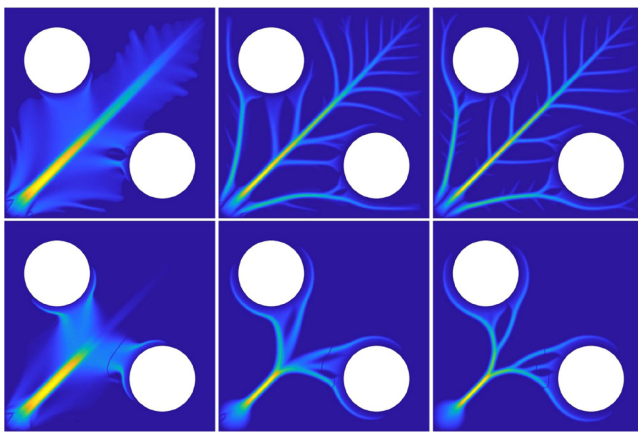


FIG. 7. The L_2 norm of the conductance vector \mathbf{m} for biological transport networks in a complex domain, initialized by sources and sinks from Eqs. (9) and (10), from (a) to (c) is shown at $t = 20, 60$, and 100 , respectively.

growth of biological networks in complex domains, simulations were conducted using sources and sinks generated by Eq. (10), alongside maintaining other initial conditions consistent with Eq. (16). As shown in Fig. 7, the evolution of the L_2 norm of the conductive vector \mathbf{m} in biological transport networks under two types of $S(\mathbf{x})$. These simulations were conducted in large circular complex domains, revealing substantial differences in network growth patterns. The first type results in the development of numerous and finer branches of biological tissues in multiple directions. The second type promotes the gradual formation of voids near complex domains as biological tissues evolve, enhancing the stability of crucial energy transfer branches while gradually dissipating unnecessary domains.

F. Multiple circular complex domain

We set the complex domain as a circle uniformly surrounding the center of the growth domain. We compare the formation of biological transport networks within this complex domain under two types of sources. The initial conditions are specified as follows:

$$\begin{aligned} G(x, y) &= \sum_{i=1}^k \frac{1}{2} \tanh \left(\frac{1}{2\sqrt{2}\epsilon} \left(\left(y - 1 - 0.58 \cos \left(\frac{2\pi i}{k} \right) \right)^2 \right. \right. \\ &\quad \left. \left. + \left(x - 1 - 0.58 \sin \left(\frac{2\pi i}{k} \right) \right)^2 \right)^{\frac{1}{2}} - 0.025 \right) + \left(1 - \frac{k}{2} \right), \\ p(x, y, 0) &= 0, \quad \mathbf{m}(x, y, 0) = (\phi(x, y, 0), 0.5\phi(x, y, 0)), \\ \phi(x, y, 0) &= 1 - \tanh \left(\frac{\sqrt{(y-1)^2 + (x-1)^2} - 0.08}{2\sqrt{2}\epsilon} \right). \end{aligned} \quad (18)$$

Here, k denotes the number of small circles, as shown in Fig. 8 the first row. Subplots (a)–(e) correspond to k values of 4, 6, 8, 12, and 16 in the complex domain G . The two types of sources are described by Eqs. (19) and (20).

$$S_1(x, y, 0) = 1.5 \left(\phi(x, y, 0) - \frac{\bar{\phi}}{1 - \bar{G}} (1 - G(x, y)) \right), \quad (19)$$

$$S_2(x, y, 0) = 1.5 (\phi(x, y, 0) - \bar{\phi}), \quad (20)$$

where $\bar{\phi} = \sum_{i=1}^{N_x} \sum_{j=1}^{N_y} \phi(x_i, y_j, 0) / (N_x \times N_y)$ and $\bar{G} = \sum_{i=1}^{N_x} \sum_{j=1}^{N_y} G(x_i, y_j) / (N_x \times N_y)$. Regarding Eq. (19), the complex domain demonstrates characteristics of energy absorption.

Energy transfer within the complex domain is constrained, predominantly occurring in the larger surrounding space. As depicted in Fig. 8, during the initial stage, the outward diffusion of energy appears nearly uniform but undergoes gradual changes due to the influence of the complex domain. Energy absorption by the complex domain profoundly impacts the growth of biological structures. The diffusion effect in the initial stages is prominent during the formation of the main trunk, which subsequently strengthens as coupling effects intensify. Energy continues to be absorbed by the complex domains, ultimately forming biological structures that extend from energy sources toward small circles around each complex domain. Increasing the number of complex domains within the same evolution time complicates the formation of the main trunk. As depicted in Figs. 8(a)–8(c), individual channels form around each small circle, posing challenges to the formation of the main trunk. In Figs. 8(d)–8(e), some circles share a main trunk and develop branches near the complex domains to transport nutrients. These observations illustrate the substantial impact of increasing the number of complex domain circles on the structure of biological transport networks. To visually compare the impact of k complex domain circles on the biological transport network, we present the L_2 norm of fluid velocity \mathbf{v} and its components v_1 and v_2 on a logarithmic scale, as shown in Fig. 9. The first and second rows display numerical values of the respective components, where colors closer to blue indicate values closer to zero. This observation reveals a pattern of thin blue lines experimentally. As the number of complex domain circles k increases, the growth of biological structures becomes more intricate, leading to a relatively slower evolution rate. Within the same evolution time, the fluid velocity throughout the domain has not yet fully stabilized, appearing complex as shown in Figs. 9(d) and 9(e).

Figure 10 illustrates the energy decay in the formation of a biological transportation network influenced by two types of sources. To provide a clearer understanding of these processes, the figure includes snapshots of the phase field variable ϕ at specific time $t = 0, 12.5, 25, 50$, and 100 . These selected time points highlight key stages in the growth process, thereby elucidating the dynamic changes throughout the evolution. For both types of sources, the subfigures depict the stable state of the biological network, where the structure remains unchanged during subsequent evolution. Specifically, Fig. 10(a) shows the growth scenario influenced by a complex domain. Due to the presence of this complex domain, the final phase field variable ϕ connects the center with small circles in the complex domain. Nutrients are continuously transported to the complex domain, without spreading to other areas. Consequently, the biological tissue lacks nutrients and does not continue to grow outward. In contrast, Fig. 10(b) illustrates the growth scenario after passing through a complex domain. The growth process continues to expand outward, ultimately forming numerous branches at the tips of the main stems. During evolution, these stems initially grow thicker, then begin to thin out, resulting in finer branches. These finer branches efficiently distribute nutrients throughout the domain, facilitating more effective energy transfer. These observations enhance

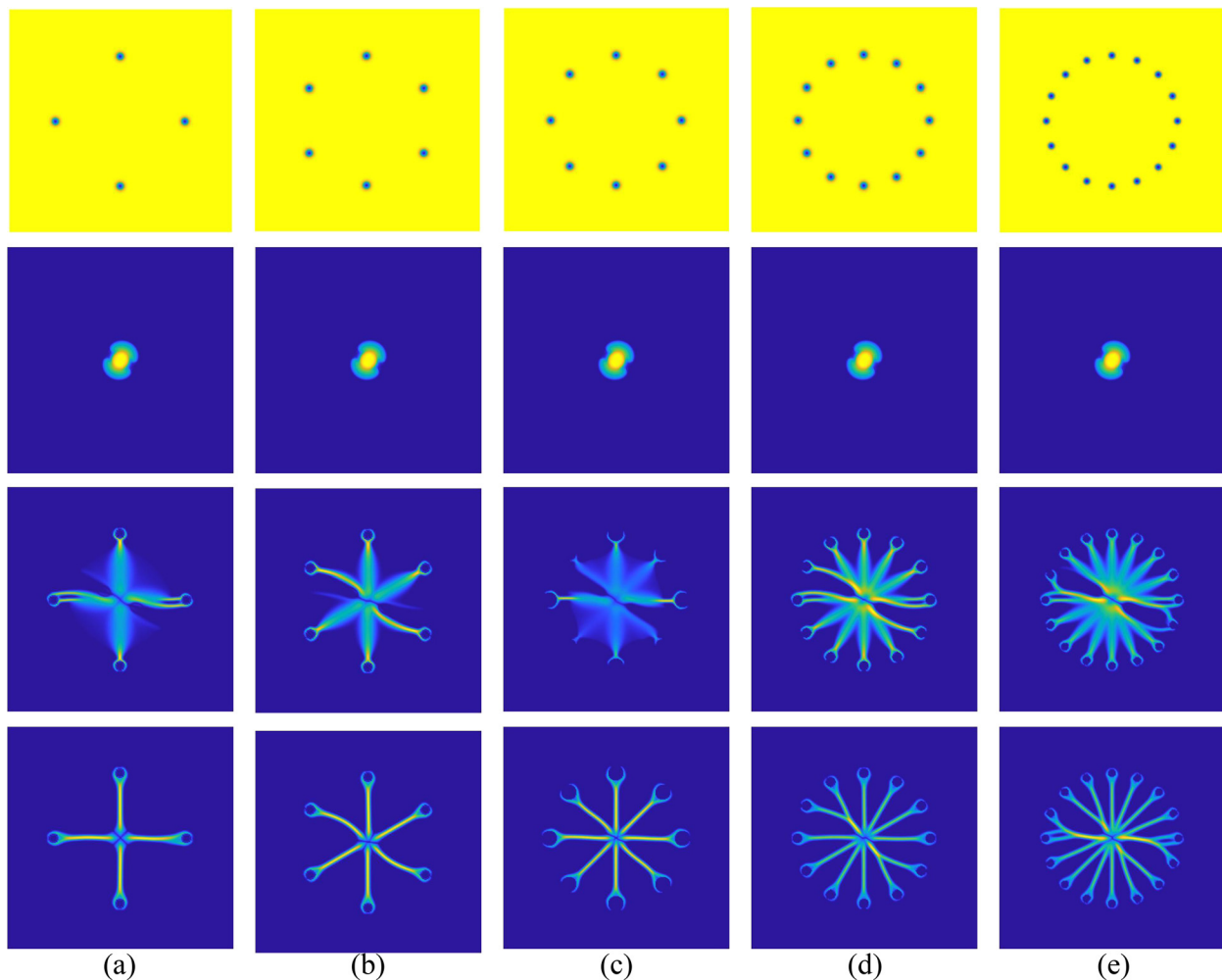


FIG. 8. The first row illustrates the complex domain G . The subsequent rows show the L_2 norm of the conductance vector \mathbf{m} for biological transport networks with sources defined by Eq. (19) at specific times $t = 1, 10$, and 100 . From (a) to (e), we use $k = 4, 6, 8, 12$, and 16 , respectively.

our understanding of the evolutionary characteristics and stable states of biological networks under different source types.

We examined the L_2 norms of both the conductivity vector \mathbf{m} and ∇p across a range of complex domains. Our emphasis was on the impact of small circular domains on biological transport networks, particularly those highlighted in red boxes in Fig. 11. In domains with four small circles, the influence in the top-right corner is minimal; the conductivity vector \mathbf{m} forms a main stem structure branching near the domain's center, as shown in Fig. 11(a). Increasing the number of small circles to 8 and 12 results in new growth points emerging after the main stem bypasses the area, leading to branching. Complex domains with 16 small circles exhibit multiple main stems, forming a more intricate branching structure. Reduced nutrient availability to each main stem, however, results in fewer and thinner branches. The formation of biological transport networks is closely correlated with ∇p . In domains with 4 small circles, the pressure gradient directs nutrient distribution away from the center. Increasing the number of small circles to 8 and 12 leads to main stem branching after bypassing

the complex domain, thereby facilitating a more balanced nutrient distribution. Despite the presence of three small circles in the bottom-right corner, domains with 16 small circles develop only two main stems, as depicted in Fig. 11(e), where one main stem bypasses the complex domain, passing between two small circles within. In summary, the quantity of small circular domains within complex areas profoundly influences the formation and branching structure of main stems.

G. Impact of complex domain density and source shape on biological structure growth

This section compares the growth dynamics of biological transport networks with two shapes of sources and sinks under sparse and dense conditions in complex domains. Dense complex domains consist of 20 small circles with a radius of 0.035, while sparse conditions involve 12 circular domains. The shapes of sources and sinks are generated by an elliptical transition function $E(x, y)$ following the form

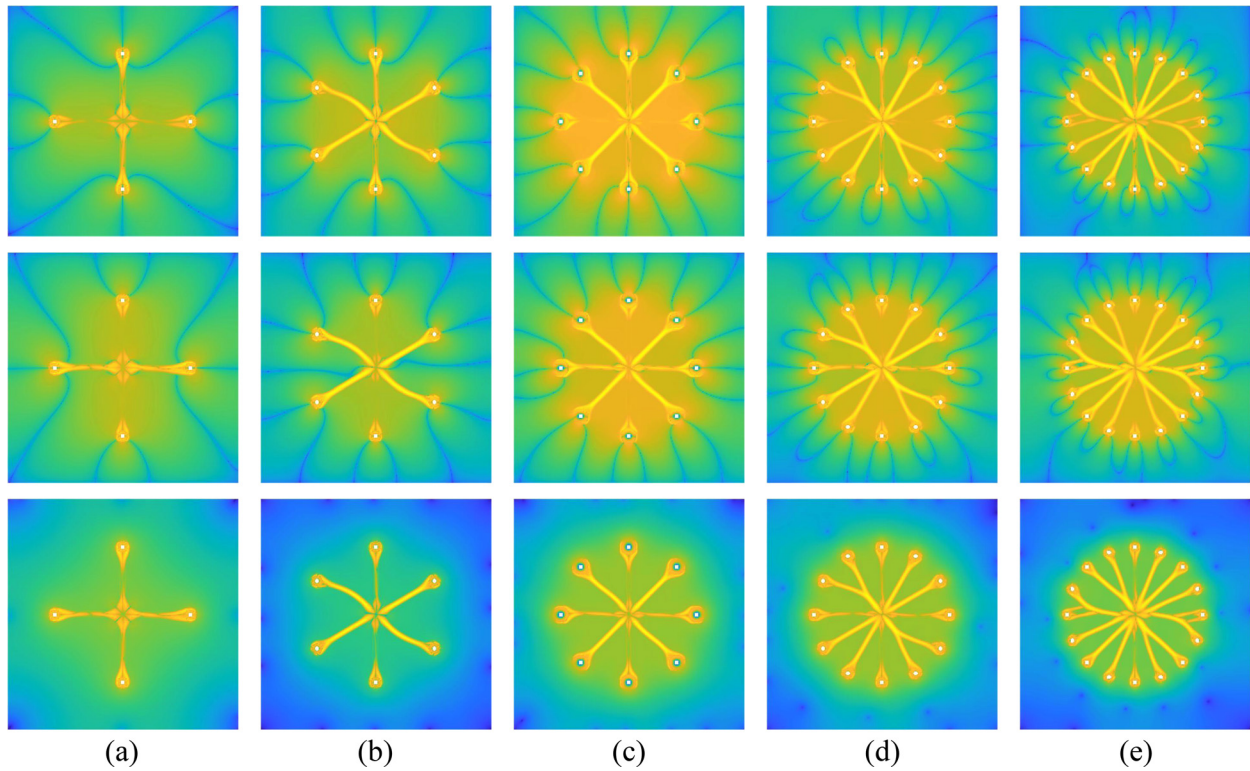


FIG. 9. Logarithmic scale representation of L_2 norms for fluid velocity components v_1 and v_2 , and the overall L_2 norm of fluid velocity v , across $k = 4, 6, 8, 12$, and 16 in the complex domain G at time $t = 100$, respectively.

$S(x, y, 0) = E(x, y) - (\bar{E}/(1 - \bar{G}))(1 - G(x, y))$, facilitating energy absorption by the complex domains. Here, $\bar{E} = \sum_{i=1}^{N_x} \sum_{j=1}^{N_y} E(x_i, y_j)$ / ($N_x \times N_y$) and $\bar{G} = \sum_{i=1}^{N_x} \sum_{j=1}^{N_y} G(x_i, y_j)$ / ($N_x \times N_y$). The ellipses $E(x, y)$ of the two shapes have major axes of 0.46 and 0.92 with minor axes of 0.030 and 0.015, respectively. As depicted in Fig. 12(a), it visually illustrates the initial configuration of sources and sinks along with

the distribution of complex domains. Additional initial conditions are set as follows:

$$\begin{aligned} \phi(x, y, 0) &= 1 - \tanh\left(\frac{\sqrt{(y-1)^2 + (x-1)^2} - 0.08}{2\sqrt{2}\epsilon}\right), \\ \mathbf{m}(x, y, 0) &= (\phi(x, y, 0), 0.5\phi(x, y, 0)), \quad p(x, y, 0) = 0. \end{aligned} \quad (21)$$

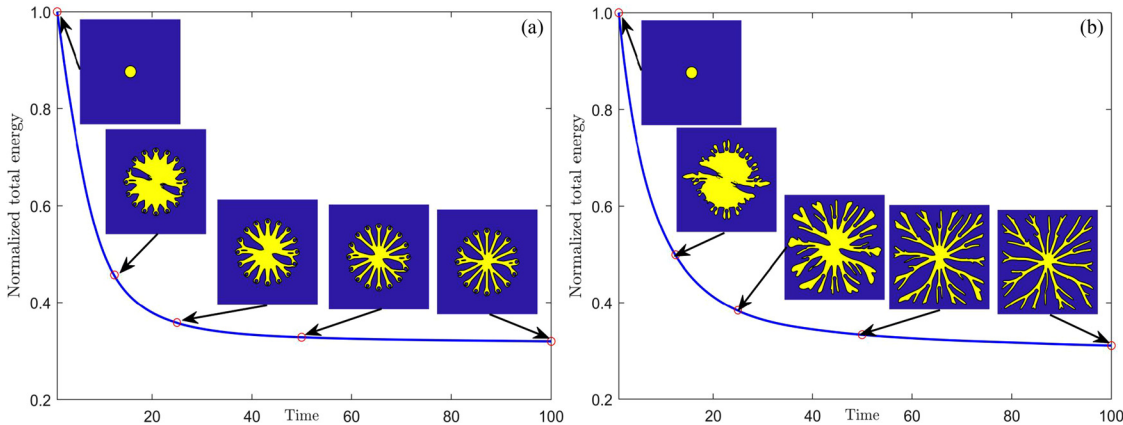


FIG. 10. The temporal evolution of the non-increasing energy of the proposed model under two different sources. Note that the modified energy has been normalized by the initial energy. The inset figures show the morphology of the phase field ϕ at specific times $t = 0, 12.5, 25, 50$, and 100 , respectively.

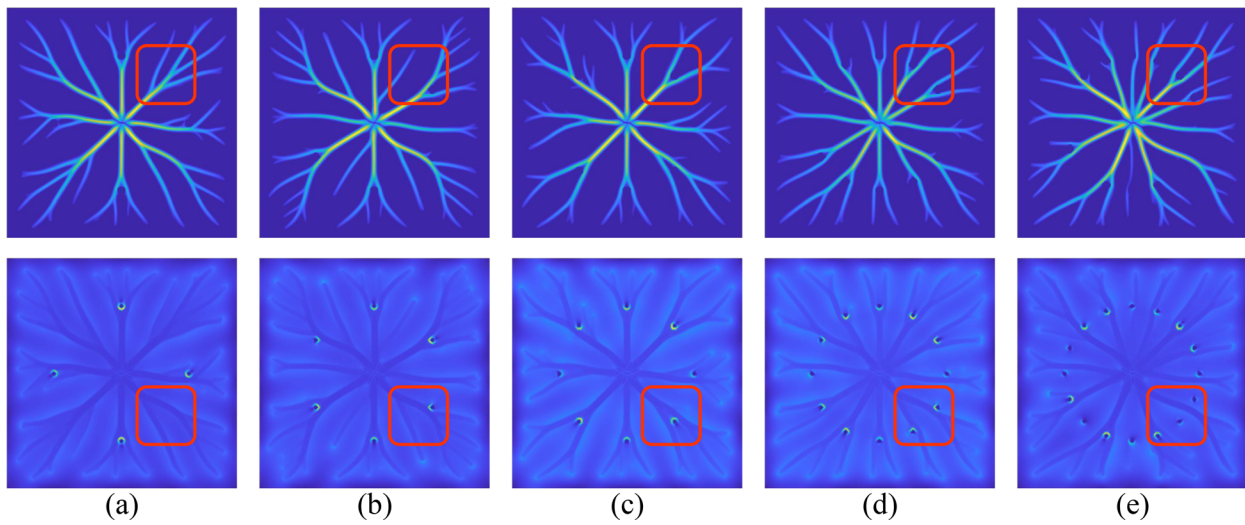


FIG. 11. The plots in the first and second rows represent the L_2 norm of the conductance vector \mathbf{m} and the L_2 norm of the pressure gradient ∇p , respectively. From (a) to (e) correspond to $k = 4, 6, 8, 12$, and 16 in the complex domain G at time $t = 100$, respectively.

The growth dynamics of biological transport networks under varying conditions exhibit notable differences. Initial growth from centrally located sources, as depicted in Fig. 12, shows similarity in the first and second rows until encountering complex domains. However, distinct

developmental outcomes arise due to the varying densities of small circular areas within these domains, highlighted in the red boxes of Fig. 12 that illustrate differences in branch formations during network development. In densely packed complex domains, a primary branch

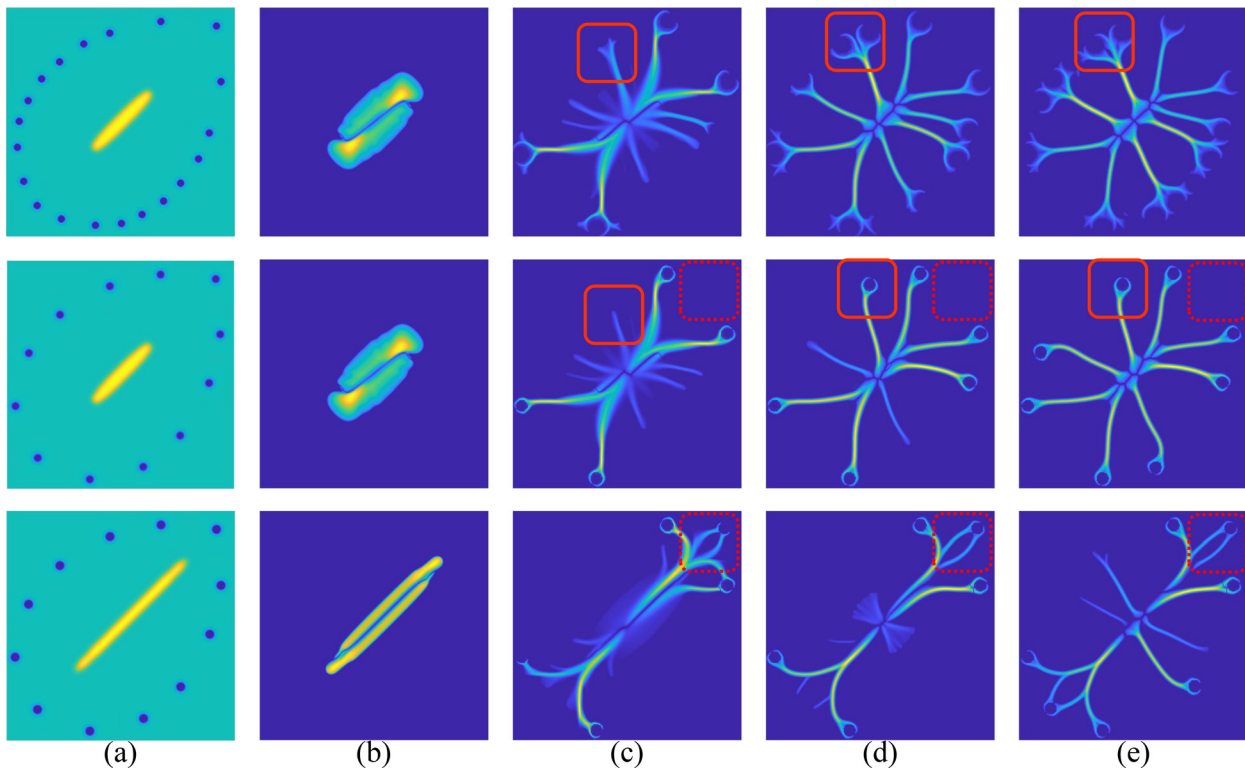


FIG. 12. The L_2 norm of the conductance vector \mathbf{m} evolves. (a) comprises three configurations: two setups with identical sources and sinks but varying regional complexities, and two setups with identical regional complexities but different sources and sinks. From (b) to (e) represent the L_2 norm of \mathbf{m} at $t = 1, 20, 50$, and 100 for the three configurations, respectively.

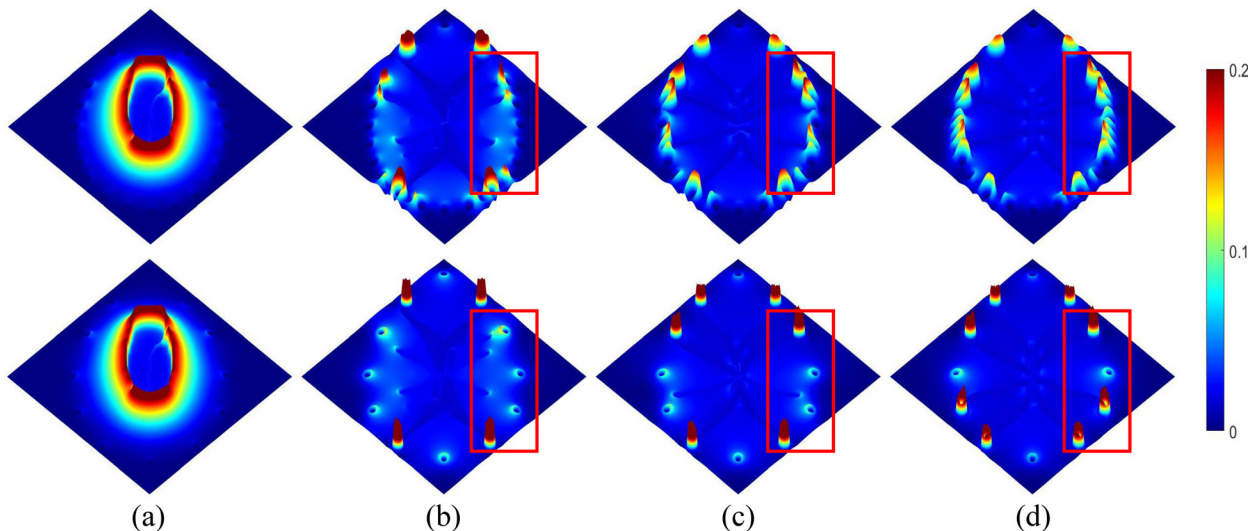


FIG. 13. The L_2 norm of the gradient of pressure ∇p at different times. From (a) to (d) depict the L_2 norm of the gradient of pressure ∇p at specific times $t = 1, 20, 50$, and 100 , on the different complex domains, respectively.

must distribute nutrients to multiple areas, promoting early branching and sustained outward growth. Conversely, in sparsely populated complex domains, a primary branch tends to supply nutrients to a single area, restricting further expansion once the main structure forms. Figure 12 also includes red dashed boxes demonstrating how various source shapes influence the growth of biological structures, especially in the top-right complex domain. The proximity of the central source to this area facilitates nutrient diffusion, promoting the formation of branching structures.

Figure 13(a) shows the initial condition at $t = 1$, where osmotic pressure in the biological transport network diffuses uniformly outward. As the biological structures form, osmotic pressure becomes influenced by the complex domains, with high-pressure differences gradually concentrating around these areas. The first row of the figure demonstrates that in densely packed complex domains, one area can quickly affect its surroundings. As the network forms, the number of complex domains with significant pressure differences increases. Conversely, in sparsely complex domains, a primary branch supplies nutrients to only one area. In this case, domains with higher osmotic pressure emerge only after the preceding area has accumulated sufficient pressure, as shown in the second row of Fig. 13. This phenomenon indicates that once certain domains accumulate enough nutrients, the excess nutrients redistribute to neighboring areas, leading to pressure differences.

V. CONCLUSION

In this study, we introduce a novel biological transport network model tailored to simulate and analyze scenarios involving obstacles and parasitic organisms encountered during the growth of biological structures in complex environments. Our model integrates phase field theory with the Cai–Hu model and incorporates two types of source terms: one simulates domains obstructing nutrient transport without energy absorption, while the other models domain obstructing and absorbing energy. Rooted in the physical principles governing biological transport networks, our study rigorously validates the model's

adherence to the law of continuous energy dissipation for continuous functions. We achieve second-order temporal accuracy by employing a Crank–Nicolson type method to control the system dynamics. Despite using a semi-implicit time integration scheme, our algorithm ensures stability, effectively addressing stiffness issues inherent in mixed systems. The discrete system derived from the phase field model is decoupled, linear, and unconditionally stable, facilitating straightforward implementation of our proposed algorithm. We conducted comprehensive numerical tests, evaluating the influence of complex domains on biological network growth, non-decreasing discrete energy, stability, convergence, and the effects of complex domain density and source shape on biological structure growth. These tests validate the efficiency, stability, and robustness of our approach. In summary, our research not only demonstrates the adherence of our biological transport network model to physical principles but also showcases its excellent performance in practical numerical tests. This study establishes a theoretical foundation and analytical framework for further investigations into the growth of biological transport networks in complex environments.

ACKNOWLEDGMENTS

Y. B. Li is supported by the National Natural Science Foundation of China (No. 12271430). The authors would like to thank the reviewers for their constructive and helpful comments regarding the revision of this article.

AUTHOR DECLARATIONS

Conflict of Interest

The authors have no conflicts to disclose.

Author Contributions

Yibao Li: Conceptualization (equal); Methodology (equal); Software (equal); Supervision (equal); Writing – review & editing (equal).

Zhixian Lv: Conceptualization (equal); Methodology (equal); Software (equal); Writing – original draft (equal). **Qing Xia:** Conceptualization (equal); Investigation (equal); Methodology (equal); Project administration (equal); Supervision (equal); Validation (equal); Writing – review & editing (equal).

DATA AVAILABILITY

Data sharing is not applicable to this article as no new data were created or analyzed in this study.

APPENDIX: UNCONDITIONAL STABILITY

We demonstrate the unconditional stability of the proposed scheme Eqs. (12). Let us define the discrete energy $\mathcal{E}_d(\phi^n, \mathbf{m}^n, p^n)$ is defined as Eq. (13) The discrete system given in Eqs. (12) preserves the energy dissipation law as follows:

$$\frac{\mathcal{E}_d(\phi^{n+1}, \mathbf{m}^{n+1}, p^{n+1}) - \mathcal{E}_d(\phi^n, \mathbf{m}^n, p^n)}{\Delta t} = - \left\| \frac{\mathbf{m}^{n+1} - \mathbf{m}^n}{\Delta t} \right\|_d^2 - \left\| \frac{\phi^{n+1} - \phi^n}{\Delta t} \right\|_d^2 \leq 0.$$

We substitute the discrete energy Eq. (13) into the left side of the equation to be proven, and after rearranging, we obtain the following:

$$\begin{aligned} \frac{\mathcal{E}_d(\phi^{n+1}, \mathbf{m}^{n+1}, p^{n+1}) - \mathcal{E}_d(\phi^n, \mathbf{m}^n, p^n)}{\Delta t} &= \frac{1}{\Delta t} \left(\left(\left(\frac{CG}{2}, \|\mathbf{m}^{n+1} \cdot \nabla_d p^{n+1}\|_d^2 \right)_d + \left(\frac{\alpha G}{2\gamma}, \|\mathbf{m}^{n+1}\|_d^{2\gamma} \right)_d + \left(\frac{CrG}{2}, \|\nabla_d p^{n+1}\|_d^2 \right)_d \right. \right. \\ &\quad \left. \left. + \frac{K}{2} \|G \nabla_d \mathbf{m}^{n+1}\|_d^2 + \left(\frac{G}{\varepsilon^2}, F(\phi^{n+1}) \right)_d + \left(\frac{\zeta G}{2}, \|\mathbf{m}^{n+1} \cdot \nabla_d \phi^{n+1}\|_d^2 \right)_d + \left(\frac{G}{2}, \|\nabla_d \phi^{n+1}\|_d^2 \right)_d \right) \right. \\ &\quad \left. - \left(\frac{K}{2} \|G \nabla_d \mathbf{m}^n\|_d^2 + \left(\frac{\alpha G}{2\gamma}, \|\mathbf{m}^n\|_d^{2\gamma} \right)_d + \left(\frac{G}{\varepsilon^2}, F(\phi^n) \right)_d + \left(\frac{CrG}{2}, \|\nabla_d p^n\|_d^2 \right)_d \right. \right. \\ &\quad \left. \left. + \left(\frac{\zeta G}{2}, \|\mathbf{m}^n \cdot \nabla_d \phi^n\|_d^2 \right)_d + \left(\frac{CG}{2}, \|\mathbf{m}^n \cdot \nabla_d p^n\|_d^2 \right)_d + \left(\frac{G}{2}, \|\nabla_d \phi^n\|_d^2 \right)_d \right) \right) \\ &= \frac{K}{2} \delta_t^+ \|G \nabla_d \mathbf{m}^n\|_d^2 + \left(\frac{\alpha G}{2\gamma}, \delta_t^+ \|\mathbf{m}^n\|_d^{2\gamma} \right)_d + \left(\frac{G}{\varepsilon^2}, \delta_t^+(F(\phi^n)) \right)_d + \left(\frac{G}{2}, \delta_t^+ \|\nabla_d \phi^n\|_d^2 \right)_d \\ &\quad + \left(\frac{\zeta G}{2}, \delta_t^+ \|\mathbf{m}^n \cdot \nabla_d \phi^n\|_d^2 \right)_d + \left(\frac{CG}{2}, \delta_t^+ \|\mathbf{m}^n \cdot \nabla_d p^n\|_d^2 \right)_d + \left(\frac{CrG}{2}, \delta_t^+ \|\nabla_d p^n\|_d^2 \right)_d. \end{aligned} \quad (\text{A1})$$

Note that we can consider the reformulation as the following parts:

$$\begin{aligned} \frac{K}{2} \delta_t^+ \|G \nabla_d \mathbf{m}^n\|_d^2 &= K \left(\nabla_d G \mathbf{m}^{n+\frac{1}{2}}, G \nabla_d \delta_t^+ \mathbf{m}^n \right)_d, \\ \left(\frac{\alpha G}{2\gamma}, \delta_t^+ \|\mathbf{m}^n\|_d^{2\gamma} \right)_d &= \left(\|\mathbf{m}^{n+\frac{1}{2}}\|_d^\gamma, \frac{\alpha G}{\gamma} \delta_t^+ \|\mathbf{m}^n\|_d^\gamma \right)_d = (\|\mathbf{m}^{n+\frac{1}{2}}\|_d^\gamma, \alpha \|\mathbf{m}^{n+\frac{1}{2}}\|_d^{\gamma-2} \cdot G \mathbf{m}^{n+\frac{1}{2}} \cdot \delta_t^+ \mathbf{m}^n)_d \\ &= (\alpha \|\mathbf{m}^{n+\frac{1}{2}}\|_d^{2(\gamma-1)} \cdot G \mathbf{m}^{n+\frac{1}{2}}, \delta_t^+ \mathbf{m}^n)_d, \\ \left(\frac{G}{\varepsilon^2}, \delta_t^+(F(\phi^n)) \right)_d &= \left(\frac{G}{\Delta t \varepsilon^2} (F(\phi^{n+1}) - F(\phi^n)), \mathbf{1} \right)_d = \left(\xi^{n+\frac{1}{2}} \frac{G}{\varepsilon^2} \frac{\delta F(\tilde{\phi}^{n+\frac{1}{2}})}{\delta \phi}, \delta_t^+ \phi^n \right)_d, \\ \left(\frac{G}{2}, \delta_t^+ \|\nabla_d \phi^n\|_d^2 \right)_d &= \left(G \nabla_d \phi^{n+\frac{1}{2}}, \nabla_d \delta_t^+ \phi^n \right)_d, \\ \left(\frac{\zeta G}{2}, \delta_t^+ \|\mathbf{m}^n \cdot \nabla_d \phi^n\|_d^2 \right)_d &= (\zeta G \mathbf{m}^{n+\frac{1}{2}} \cdot \nabla_d \phi^{n+\frac{1}{2}}, \tilde{\mathbf{m}}^{n+\frac{1}{2}} \cdot \nabla_d \delta_t^+ \phi^n + \delta_t^+ \mathbf{m}^n \cdot \nabla_d \tilde{\phi}^{n+\frac{1}{2}})_d \\ &= (\zeta G (\mathbf{m}^{n+\frac{1}{2}} \otimes \tilde{\mathbf{m}}^{n+\frac{1}{2}}) \nabla_d \phi^{n+\frac{1}{2}}, \nabla_d \delta_t^+ \phi^n)_d - (\zeta (G \mathbf{m}^{n+\frac{1}{2}} \cdot \nabla_d \phi^{n+\frac{1}{2}}) \nabla_d \tilde{\phi}^{n+\frac{1}{2}}, \delta_t^+ \mathbf{m}^n)_d, \\ \left(\frac{CG}{2}, \delta_t^+ \|\mathbf{m}^n \cdot \nabla_d p^n\|_d^2 \right)_d &= C (G \mathbf{m}^{n+\frac{1}{2}} \cdot \nabla_d p^{n+\frac{1}{2}}, \tilde{\mathbf{m}}^{n+\frac{1}{2}} \cdot \nabla_d \delta_t^+ \phi^n)_d \end{aligned}$$

$$p^n + \delta_t^+ \mathbf{m}^n \cdot \nabla_d \tilde{p}^{n+\frac{1}{2}})_d = C(G\mathbf{m}^{n+\frac{1}{2}} \otimes \tilde{\mathbf{m}}^{n+\frac{1}{2}}) \nabla_d p^{n+\frac{1}{2}}, \nabla_d \delta_t^+ p^n)_d + C(G\mathbf{m}^{n+\frac{1}{2}} \cdot \nabla_d p^{n+\frac{1}{2}}, \delta_t^+ \mathbf{m}^n \cdot \nabla_d \tilde{p}^{n+\frac{1}{2}})_d,$$

$$\left(\frac{CrG}{2}, \delta_t^+ \|\nabla_d p^n\|_d^2\right)_d = C(rG \nabla_d p^{n+\frac{1}{2}}, \nabla_d \delta_t^+ p^n)_d.$$

We compute the discrete inner product of Eq. (12a) with $\delta_t^+ \phi^n = (\phi^{n+1} - \phi^n)/\Delta t$, Eq. (12c) with $\delta_t^+ p^n = (p^{n+1} - p^n)/\Delta t$, and Eq. (12d) with $\delta_t^+ \mathbf{m}^n = (\mathbf{m}^{n+1} - \mathbf{m}^n)/\Delta t$. Therefore, Eq. (A1) can be rewritten as follows:

$$\begin{aligned} \frac{\mathcal{E}_d(\phi^{n+1}, \mathbf{m}^{n+1}, p^{n+1}) - \mathcal{E}_d(\phi^n, \mathbf{m}^n, p^n)}{\Delta t} &= K \left(\nabla_d G \mathbf{m}^{n+\frac{1}{2}}, G \nabla_d \delta_t^+ \mathbf{m}^n \right)_d + CG \left(rI \nabla_d p^{n+\frac{1}{2}}, \nabla_d \delta_t^+ p^n \right)_d + \left(G \nabla_d \phi^{n+\frac{1}{2}}, \nabla_d \delta_t^+ \phi^n \right)_d \\ &\quad + C(G\mathbf{m}^{n+\frac{1}{2}} \cdot \nabla_d p^{n+\frac{1}{2}}, \delta_t^+ \mathbf{m}^n \cdot \nabla_d \tilde{p}^{n+\frac{1}{2}})_d + C(G\mathbf{m}^{n+\frac{1}{2}} \otimes \tilde{\mathbf{m}}^{n+\frac{1}{2}}) \nabla_d p^{n+\frac{1}{2}}, \nabla_d \delta_t^+ p^n)_d \\ &\quad - \left(\zeta \left(G\mathbf{m}^{n+\frac{1}{2}} \cdot \nabla_d \phi^{n+\frac{1}{2}} \right) \cdot \nabla_d \tilde{\phi}^{n+\frac{1}{2}}, \delta_t^+ \mathbf{m}^n \right)_d + \zeta \left(G(\mathbf{m}^{n+\frac{1}{2}} \otimes \tilde{\mathbf{m}}^{n+\frac{1}{2}}) \nabla_d \phi^{n+\frac{1}{2}}, \nabla_d \delta_t^+ \phi^n \right)_d \\ &\quad + \left(\xi^{n+\frac{1}{2}} \frac{G}{\varepsilon^2} \delta F \left(\frac{\tilde{\phi}^{n+\frac{1}{2}}}{\delta \phi} \right) \delta_t^+ \phi^n \right)_d + \alpha \left(\|\mathbf{m}^{n+\frac{1}{2}}\|_d^{2(\gamma-1)} \cdot G\mathbf{m}^{n+\frac{1}{2}}, \delta_t^+ \mathbf{m}^n \right)_d \\ &= \left(\xi^{n+\frac{1}{2}} \frac{G}{\varepsilon^2} \frac{\delta F(\tilde{\phi}^{n+\frac{1}{2}})}{\delta \phi}, \delta_t^+ \phi^n \right)_d + \left(G \nabla_d \phi^{n+\frac{1}{2}}, \nabla_d \delta_t^+ \phi^n \right)_d + \zeta \left(G(\mathbf{m}^{n+\frac{1}{2}} \otimes \tilde{\mathbf{m}}^{n+\frac{1}{2}}) \nabla_d \phi^{n+\frac{1}{2}}, \nabla_d \delta_t^+ \phi^n \right)_d \\ &\quad - (K \nabla_d \cdot (G^2 \nabla_d \mathbf{m}^{n+\frac{1}{2}}), \delta_t^+ \mathbf{m}^n)_d + C(G\mathbf{m}^{n+\frac{1}{2}} \cdot \nabla_d p^{n+\frac{1}{2}}, \delta_t^+ \mathbf{m}^n \cdot \nabla_d \tilde{p}^{n+\frac{1}{2}})_d \\ &\quad + \alpha \left(\|\mathbf{m}^{n+\frac{1}{2}}\|_d^{2(\gamma-1)} \cdot G\mathbf{m}^{n+\frac{1}{2}}, \delta_t^+ \mathbf{m}^n \right)_d - \left(\zeta \left(G\mathbf{m}^{n+\frac{1}{2}} \cdot \nabla_d \phi^{n+\frac{1}{2}} \right) \cdot \nabla_d \tilde{\phi}^{n+\frac{1}{2}}, \delta_t^+ \mathbf{m}^n \right)_d \\ &= -\|\delta_t^+ \phi^n\|_d^2 - \|\delta_t^+ \mathbf{m}^n\|_d^2 \leq 0. \end{aligned} \tag{A2}$$

Here, the proof is completed.

REFERENCES

- ¹D. Hu and D. Cai, "Adaptation and optimization of biological transport networks," *Phys. Rev. Lett.* **111**, 138701 (2013).
- ²F. Patino-Ramirez and C. Arson, "Transportation networks inspired by leaf venation algorithms," *Bioinspir. Biomim.* **15**, 036012 (2020).
- ³R. S. Udan, J. C. Culver, and M. E. Dickinson, "Understanding vascular development," *Wiley Interdiscip. Rev.* **2**, 327–346 (2013).
- ⁴A. Chandrasekhar and S. Navlakha, "Neural arbors are Pareto optimal," *Proc. R Soc. B* **286**, 20182727 (2019).
- ⁵D. Hu and D. Cai, "An optimization principle for initiation and adaptation of biological transport networks," *Commun. Math. Sci.* **17**, 1427–1436 (2019).
- ⁶G. Weng, U. S. Bhalla, and R. Iyengar, "Complexity in biological signaling systems," *Science* **284**, 92–96 (1999).
- ⁷E. L. Johnson, M. C. H. Wu, F. Xu, N. M. Wiese, M. R. Rajanna, A. J. Herrema, B. Ganapathysubramanian, T. J. R. Hughes, M. S. Sacks, and M.-C. Hsu, "Thinner biological tissues induce leaflet flutter in aortic heart valve replacements," *Proc. Natl. Acad. Sci. U. S. A.* **117**, 19007–19016 (2020).
- ⁸M. HosseiniMehr, J. P. Tomala, C. Vuik, M. A. Kobaisi, and H. Hajibeygi, "Projection-based embedded discrete fracture model (pEDFM) for flow and heat transfer in real-field geological formations with hexahedral corner-point grids," *Adv. Water Resour.* **159**, 104091 (2022).
- ⁹V. Shannugam, O. Das, K. Babu, U. Marimuthu, A. Veerasimman, D. J. Johnson, R. E. Neisany, M. S. Hedenqvist, S. Ramakrishna, and F. Berto, "Fatigue behaviour of fdm-3d printed polymers, polymeric composites and architected cellular materials," *Int. J. Fatigue* **143**, 106007 (2021).
- ¹⁰K. Makki, A. Bohi, A. C. Ogier, and M. E. Bellemare, "A new geodesic-based feature for characterization of 3D shapes: application to soft tissue organ temporal deformations," *2020 25th International Conference on Pattern Recognition (ICPR)*, (IEEE, 2021), pp. 3822–3828.
- ¹¹P. K. Smolarkiewicz, J. Szmelter, and F. Xiao, "Simulation of all-scale atmospheric dynamics on unstructured meshes," *J. Comput. Phys.* **322**, 267–287 (2016).
- ¹²M. J. Mitchell and M. R. King, "Physical biology in cancer. 3. the role of cell glycocalyx in vascular transport of circulating tumor cells," *Am. J. Physiol., Cell Physiol.* **306**, 89–97 (2014).
- ¹³M. P. Czubryt, "Common threads in cardiac fibrosis, infarct scar formation, and wound healing," *Fibrog. Tissue Repair* **5**, 1–11 (2012).
- ¹⁴M. W. Dewhirst and T. W. Secomb, "Transport of drugs from blood vessels to tumour tissue," *Nat. Rev. Cancer* **17**, 738–750 (2017).
- ¹⁵J. Liu, M. Li, Z. Luo, L. Dai, X. Guo, and K. Cai, "Design of nanocarriers based on complex biological barriers in vivo for tumor therapy," *Nano Today* **15**, 56–90 (2017).
- ¹⁶M. B. Ghorbel, D. Rodriguez-Duarte, H. Ghazzai, M. J. Hossain, and H. Menouar, "Joint position and travel path optimization for energy efficient wireless data gathering using unmanned aerial vehicles," *IEEE Trans. Veh. Technol.* **68**, 2165–2175 (2019).
- ¹⁷T. J. Marini, K. Chughtai, Z. Nuffer, S. K. Hobbs, and K. Kaproth-Joslin, "Blood finds a way: Pictorial review of thoracic collateral vessels," *Insights Imaging* **10**(1), 8 (2019).
- ¹⁸R. Zi, L. Zhao, Q. Fang, X. Qian, F. Fang, and C. Fan, "Path analysis of the effects of hydraulic conditions, soil properties and plant roots on the soil detachment capacity of karst hillslopes," *Catena* **228**, 107177 (2023).
- ¹⁹Z. Chen, L.-T. Zhu, and Z.-H. Luo, "Characterizing flow and transport in biological vascular systems: A review from physiological and chemical engineering perspectives," *Ind. Eng. Chem. Res.* **63**, 4–36 (2023).
- ²⁰A. V. Melkikh and M. Sutormina, "Intra-and intercellular transport of substances: Models and mechanisms," *Prog. Biophys. Mol. Biol.* **150**, 184–202 (2020).
- ²¹A. S. Nair, S. Abhyankar, S. Peles, and P. Ranganathan, "Computational and numerical analysis of ac optimal power flow formulations on large-scale power grids," *Electr. Power Syst. Res.* **202**, 107594 (2022).
- ²²X. Song, Q. Xia, J. Kim, and Y. Li, "An unconditional energy stable data assimilation scheme for Navier-Stokes-Cahn-Hilliard equations with local discretized observed data," *Comput. Math. Appl.* **164**, 21–33 (2024).

- ²³R. Wang, J. Lu, Y. Jiang, and F. A. Dijkstra, "Carbon efficiency for nutrient acquisition (CENA) by plants: Role of nutrient availability and microbial symbionts," *Plant Soil* **476**, 289–300 (2022).
- ²⁴J. Zhao, P. Seeluangsawat, and Q. Wang, "Modeling antimicrobial tolerance and treatment of heterogeneous biofilms," *Math. Biosci.* **282**, 1–15 (2016).
- ²⁵D. Fang, S. Jin, P. Markowich, and B. Perthame, "Implicit and semi-implicit numerical schemes for the gradient flow of the formation of biological transport networks," *SMAI J. Comput. Math.* **5**, 229–249 (2020).
- ²⁶S. Guo, C. Li, X. Li, and L. Mei, "Energy-conserving and time-stepping-varying ESAV-Hermite-Galerkin spectral scheme for nonlocal Klein-Gordon-Schrödinger system with fractional Laplacian in unbounded domains," *J. Comput. Phys.* **458**, 111096 (2022).
- ²⁷W. Chen, J. Jing, Q. Liu, C. Wang, and X. Wang, "Convergence analysis of a second order numerical scheme for the Flory-Huggins-Cahn-Hilliard-Navier-Stokes system," *J. Comput. Appl. Math.* **450**, 115981 (2024).
- ²⁸T. G. Anderson, H. Zhu, and S. Veerapaneni, "A fast, high-order scheme for evaluating volume potentials on complex 2D geometries via area-to-line integral conversion and domain mappings," *J. Comput. Phys.* **472**, 111688 (2023).
- ²⁹F. S. Costabal, S. Pezzuto, and P. Perdikaris, " δ -pins: Physics-informed neural networks on complex geometries," *Eng. Appl. Artif. Intell.* **127**, 107324 (2024).
- ³⁰C. Wang, J. Wang, Z. Xia, and L. Xu, "Optimal error estimates of a second-order projection finite element method for magnetohydrodynamic equations," *arXiv:2011.14511* (2021).
- ³¹X. Li, J. Shen, and Z. Liu, "New SAV-pressure correction methods for the Navier-Stokes equations: Stability and error analysis," *Math. Comput.* **91**, 141–167 (2021).
- ³²X. Li and J. Shen, "Stability and error estimates of the SAV Fourier-spectral method for the phase field crystal equation," *Adv. Comput. Math.* **46**, 1–20 (2020).
- ³³C. Wang, J. Wang, S. M. Wise, Z. Xia, and L. Xu, "Convergence analysis of a temporally second-order accurate finite element scheme for the Cahn-Hilliard-magnetohydrodynamics system of equations," *J. Comput. Appl. Math.* **436**, 115409 (2024).
- ³⁴B. Jiang, Q. Xia, J. Kim, and Y. Li, "Efficient second-order accurate scheme for fluid-surfactant systems on curved surfaces with unconditional energy stability," *Commun. Nonlinear Sci. Numer. Simul.* **135**, 108054 (2024).
- ³⁵J. Long, C. Luo, Q. Yu, and Y. Li, "An unconditional stable compact fourth-order finite difference scheme for three dimensional Allen-Cahn equation," *Comput. Math. Appl.* **77**, 1042–1054 (2019).
- ³⁶J. Zhao, Q. Wang, and X. Yang, "Numerical approximations for a phase field dendritic crystal growth model based on the invariant energy quadratization approach," *Numer. Meth. Eng.* **110**, 279–300 (2017).
- ³⁷B. Xia, C. Mei, Q. Yu, and Y. Li, "A second order unconditionally stable scheme for the modified phase field crystal model with elastic interaction and stochastic noise effect," *Comput. Methods Appl. Mech. Eng.* **363**, 112795 (2020).
- ³⁸Q. Xia, J. Yang, J. Kim, and Y. Li, "On the phase field based model for the crystalline transition and nucleation within the Lagrange multiplier framework," *J. Comput. Phys.* **513**, 113158 (2024).
- ³⁹Q. Xia, J. Zhu, Q. Yu, J. Kim, and Y. Li, "Triply periodic minimal surfaces based topology optimization for the hydrodynamic and convective heat transfer," *Commun. Nonlinear Sci. Numer. Simul.* **131**, 107819 (2024).
- ⁴⁰Y. Li, Q. Xia, S. Kang, S. Kwak, and J. Kim, "A practical algorithm for the design of multiple-sized porous scaffolds with triply periodic structures," *Math. Comput. Simul.* **220**, 481–495 (2024).
- ⁴¹C. Qiu, B. Wang, N. Zhang, S. Zhang, J. Liu, D. Walker, Y. Wang, H. Tian, T. R. Shroud, Z. Xu *et al.*, "Transparent ferroelectric crystals with ultrahigh piezoelectricity," *Nature* **577**, 350–354 (2020).
- ⁴²Y. Li, K. Wang, Q. Yu, Q. Xia, and J. Kim, "Unconditionally energy stable schemes for fluid-based topology optimization," *Commun. Nonlinear Sci. Numer. Simul.* **111**, 106433 (2022).
- ⁴³H. Chen, H. Leng, D. Wang, and X.-P. Wang, "An efficient threshold dynamics method for topology optimization for fluids," *arXiv:1812.09437* (2018).
- ⁴⁴H. Chen and X.-P. Wang, "A one-domain approach for modeling and simulation of free fluid over a porous medium," *J. Comput. Phys.* **259**, 650–671 (2014).
- ⁴⁵Q. Yu and Y. Li, "A second-order unconditionally energy stable scheme for phase-field based multimaterial topology optimization," *Comput. Methods Appl. Mech. Eng.* **405**, 115876 (2023).
- ⁴⁶M. Yang, L. Wang, and W. Yan, "Phase-field modeling of grain evolutions in additive manufacturing from nucleation, growth, to coarsening," *Npj Comput. Mater.* **7**, 56 (2021).
- ⁴⁷Y. Li, K. Qin, Q. Xia, and J. Kim, "A second-order unconditionally stable method for the anisotropic dendritic crystal growth model with an orientation-field," *Appl. Numer. Math.* **184**, 512–526 (2023).
- ⁴⁸X. Li and J. Shen, "Efficient linear and unconditionally energy stable schemes for the modified phase field crystal equation," *Sci. China Math.* **65**, 2201–2218 (2021).
- ⁴⁹Q. Xia, J. Yang, and Y. Li, "On the conservative phase-field method with the n-component incompressible flows," *Phys. Fluids* **35**, 012120 (2023).
- ⁵⁰J. Yang and J. Kim, "Phase-field simulation of multiple fluid vesicles with a consistently energy-stable implicit-explicit method," *Comput. Methods Appl. Mech. Eng.* **417**, 116403 (2023).
- ⁵¹R. Alessi and F. Freddi, "Failure and complex crack patterns in hybrid laminates: A phase-field approach," *Composites, Part B* **179**, 107256 (2019).
- ⁵²K. Dayal and K. Bhattacharya, "A real-space non-local phase-field model of ferroelectric domain patterns in complex geometries," *Acta Mater.* **55**, 1907–1917 (2007).
- ⁵³J. Yang, Z. Tan, J. Wang, and J. Kim, "Modified diffuse interface fluid model and its consistent energy-stable computation in arbitrary domains," *J. Comput. Phys.* **488**, 112216 (2023).
- ⁵⁴Q. Xia, X. Jiang, and Y. Li, "A modified and efficient phase field model for the biological transport network," *J. Comput. Phys.* **488**, 112192 (2023).
- ⁵⁵C. D. Murray, "The physiological principle of minimum work: I. the vascular system and the cost of blood volume," *Proc. Natl. Acad. Sci. U. S. A.* **12**, 207–214 (1926).
- ⁵⁶P. Dimitrov and S. W. Zucker, "A constant production hypothesis guides leaf venation patterning," *Proc. Natl. Acad. Sci. U. S. A.* **103**(103), 9363–9368 (2006).
- ⁵⁷K. Ljung, R. P. Bhalerao, and G. Sandberg, "Sites and homeostatic control of auxin biosynthesis in *Arabidopsis* during vegetative growth," *Plant J.* **28**, 465–474 (2001).
- ⁵⁸Q. Hong, J. Zhao, and Q. Wang, "Energy-production-rate preserving numerical approximations to network generating partial differential equations," *Comput. Math. Appl.* **84**, 148–165 (2021).
- ⁵⁹Q. Cheng, J. Shen, and C. Wang, "Unique solvability and error analysis of the Lagrange multiplier approach for gradient flows," *arXiv:2405.03415* (2024).
- ⁶⁰B. Li and Y. Li, "Global existence and eventual smoothness in a 2-D parabolic-elliptic system arising from ion transport networks," *J. Differ. Equations* **305**, 1–44 (2021).
- ⁶¹J. A. Carrillo, J. Li, and Z. A. Wang, "Boundary spike-layer solutions of the singular Keller-Segel system: Existence and stability," *Proc. London Math. Soc.* **122**, 42–68 (2021).
- ⁶²B. Li and L. Xie, "Global dynamics and zero-diffusion limit of a parabolic-elliptic-parabolic system for ion transport networks," *Nonlinear Anal. Real World Appl.* **60**, 103304 (2021).
- ⁶³J. Guo, C. Wang, S. M. Wise, and X. Yue, "An H^2 convergence of a second-order convex-splitting, finite difference scheme for the three-dimensional Cahn-Hilliard equation," *Commun. Math. Sci.* **14**, 489–515 (2016).
- ⁶⁴A. E. Diegel, C. Wang, and S. M. Wise, "Stability and convergence of a second-order mixed finite element method for the Cahn-Hilliard equation," *IMA J. Numer. Anal.* **36**, 1867–1897 (2016).
- ⁶⁵K. Cheng, C. Wang, S. M. Wise, and X. Yue, "A second-order, weakly energy-stable pseudo-spectral scheme for the Cahn-Hilliard equation and its solution by the homogeneous linear iteration method," *J. Sci. Comput.* **69**, 1083–1114 (2016).
- ⁶⁶J. Haskovec, P. Markowich, and B. Perthame, "Mathematical analysis of a PDE system for biological network formation," *Commun. Partial Differ. Equations* **40**, 918–956 (2015).